Monthly Notices of the ROYAL ASTRONOMICAL SOCIETY

MNRAS **498,** 4906–4923 (2020) doi:10.1093/mnras/staa2719
Advance Access publication 2020 September 8

Which feedback mechanisms dominate in the high-pressure environment of the central molecular zone?

Ashley T. Barnes [1]★ Steven N. Longmore,[2] James E. Dale,[3] Mark R. Krumholz [4,5] J. M. Diederik Kruijssen [6] and Frank Bigiel[1]

[1]*Argelander-Institut für Astronomie, Universität Bonn, Auf dem Hügel 71, D-53121 Bonn, Germany*
[2]*Astrophysics Research Institute, Liverpool John Moores University, 146 Brownlow Hill, Liverpool L3 5RF, UK*
[3]*Centre for Astrophysics Research, University of Hertfordshire, Hatfield AL10 9AB, UK*
[4]*Research School of Astronomy and Astrophysics, Australian National University, Canberra, ACT 2611, Australia*
[5]*ARC Centre of Excellence for Astronomy in Three Dimensions (ASTRO-3D), Canberra, ACT 2601, Australia*
[6]*Astronomisches Rechen-Institut, Zentrum für Astronomie der Universität Heidelberg, Mönchhofstraße 12-14, D-69120 Heidelberg, Germany*

Accepted 2020 September 3. Received 2020 September 3; in original form 2020 July 14

ABSTRACT

Supernovae (SNe) dominate the energy and momentum budget of stellar feedback, but the efficiency with which they couple to the interstellar medium (ISM) depends strongly on how effectively early, pre-SN feedback clears dense gas from star-forming regions. There are observational constraints on the magnitudes and time-scales of early stellar feedback in low ISM pressure environments, yet no such constraints exist for more cosmologically typical high ISM pressure environments. In this paper, we determine the mechanisms dominating the expansion of H II regions as a function of size-scale and evolutionary time within the high-pressure ($P/k_{\rm B} \sim 10^{7-8}\,{\rm K\,cm^{-3}}$) environment in the inner 100 pc of the Milky Way. We calculate the thermal pressure from the warm ionized ($P_{\rm H\,II}$; 10^4 K) gas, direct radiation pressure ($P_{\rm dir}$), and dust processed radiation pressure ($P_{\rm IR}$). We find that (1) $P_{\rm dir}$ dominates the expansion on small scales and at early times (0.01–0.1 pc; <0.1 Myr); (2) the expansion is driven by $P_{\rm HII}$ on large scales at later evolutionary stages (>0.1 pc; >1 Myr); (3) during the first $\lesssim$ 1 Myr of growth, but not thereafter, either $P_{\rm IR}$ or stellar wind pressure likely make a comparable contribution. Despite the high confining pressure of the environment, natal star-forming gas is efficiently cleared to radii of several pc within $\sim$ 2 Myr, i.e. before the first SNe explode. This 'pre-processing' means that subsequent SNe will explode into low density gas, so their energy and momentum will efficiently couple to the ISM. We find the H II regions expand to a radius of $\sim$ 3 pc, at which point they have internal pressures equal with the surrounding external pressure. A comparison with H II regions in lower pressure environments shows that the maximum size of all H II regions is set by pressure equilibrium with the ambient ISM.

Key words: stars: formation – ISM: clouds – Galaxy: centre.

1 INTRODUCTION

Throughout their short lifetimes, high-mass stars (>8 $M_\odot$) inject large amounts of energy and momentum into their host environments through a variety of feedback processes (e.g. Krumholz et al. 2014). The most potentially disruptive of these feedback mechanisms occurs when the stars eventually die, exploding as supernovae (SNe). Indeed, SNe are thought to play a major role in the self-regulation of star formation in galaxies through their contribution to the total energy and momentum budget of the interstellar medium (ISM; McKee & Ostriker 1977; Mac Low & Klessen 2004; Klessen & Glover 2016). As the rate of cooling in the ISM is proportional to the gas density squared, the efficiency with which SNe inject energy and momentum into the local galactic environment strongly depends on the density distribution of the gas into which they explode (see Girichidis et al. 2016 and references therein). For example, SNe that explode within dense molecular clouds may be limited to disrupting their natal gas clouds, whilst SNe that explode into lower density environments can drive hot expanding bubbles to much larger distances (tens to hundreds of pc) and influence galactic scale processes (e.g. kpc-scale galactic outflows; Veilleux, Cecil & Bland-Hawthorn 2005; Agertz et al. 2013; Stinson et al. 2013; Keller, Kruijssen & Wadsley 2020; Veilleux et al. 2020). Feedback from the pre-SNe stages of high-mass stars plays a significant role in determining the environment into which SNe subsequently explode. Simulations have long predicted that this 'pre-processing' can potentially even destroy the host molecular cloud before the first SN explosion (e.g. Dale, Ercolano & Bonnell 2012, 2013), and observations of molecular clouds and H II regions in nearby galaxies now show that pre-SN feedback is primarily responsible for the destruction of molecular clouds across the local galaxy population (Kruijssen et al. 2019b; Chevance et al. 2020b,c). Studying the effects of these earliest stages of stellar feedback on their environment is then crucial to quantifying the contribution of SNe in driving the galaxy-scale energy and momentum cycle of the ISM in galaxies. In light of this, significant observational effort has been invested to better disentangle and quantify the effect of various feedback mechanisms within young

★ E-mail: ashleybarnes.astro@gmail.com

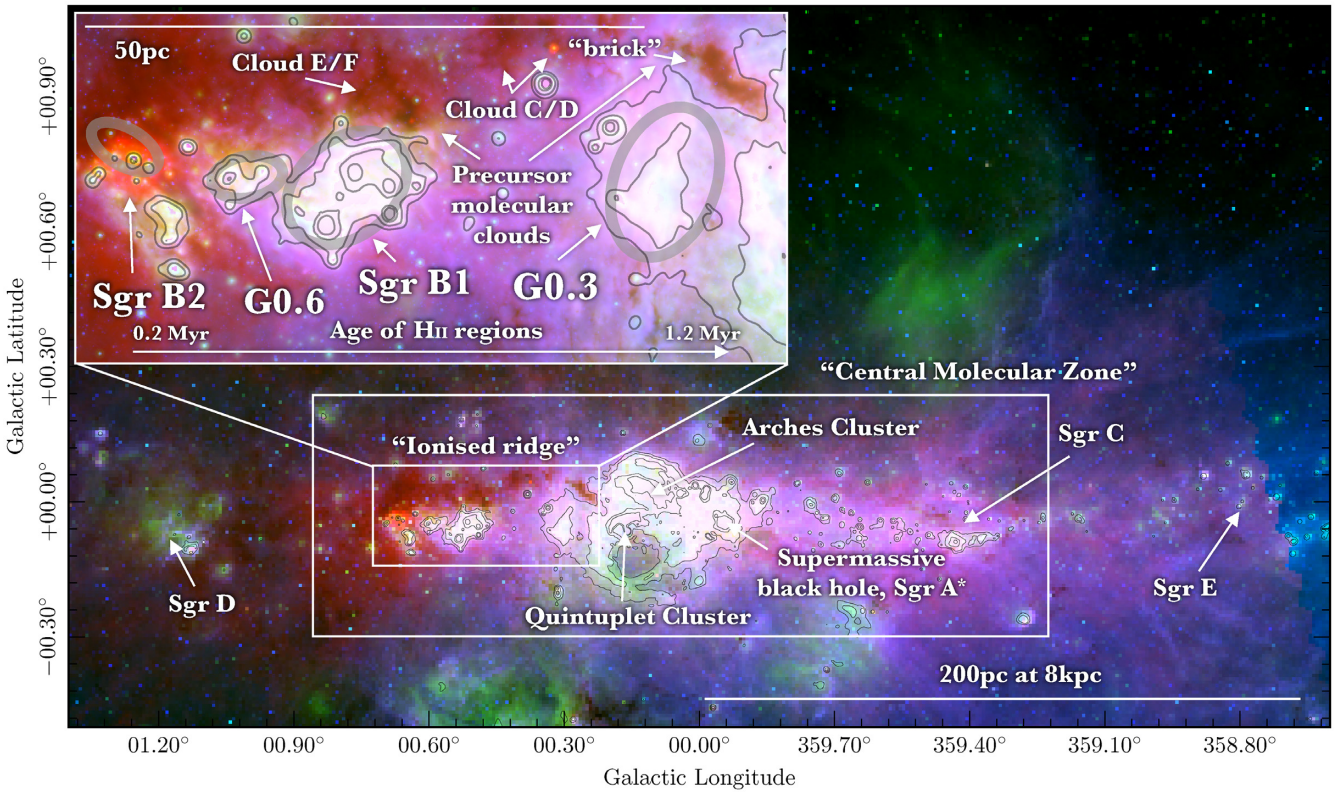

Figure 1. A three colour image of the Galactic Centre. In this image, red is 70 μm emission from *Herschel* Hi-GAL (Molinari et al. 2010), green is 24 μm emission from *Spitzer* MIPSGAL (Carey et al. 2009), and blue is 8 μm emission from *Spitzer* GLIMPSE (Churchwell et al. 2009). We label sources of interest throughout this region, such as the prominent massive clusters (Arches and Quintuplet; e.g. Espinoza, Selman & Melnick 2009; Harfst, Portegies Zwart & Stolte 2010), the supermassive black hole (Sgr A∗; e.g. Gravity Collaboration 2018), and several prominent H II regions (e.g. Sgr E; Anderson et al. 2020). Rectangles show the approximate regions of the Central Molecular Zone (or CMZ) and the dust-ridge. The 24 μm emission map is also overlaid in contours of 400, 1000, and 1500 MJy sr^{-1}, which have been chosen to best highlight the sources of interest. The inset in the upper left shows a zoom-in of the ionized-ridge region, which contains the sources Sgr B2, G0.6, Sgr B1, and G0.3 that we study in this work. In the zoom-in panel, we also label molecular clouds that are thought to represent the initial conditions of the H II regions (see Section 3.2). Labels at the bottom of the zoom-in panel give the approximate ages of the H II regions based on the predictions from an orbital model (increasing age from left to right; Longmore et al. 2013b; Kruijssen, Dale & Longmore 2015). In the lower right of the main panel and upper left of the zoom-in panel we show scale-bars representing projected lengths of ∼200 pc and ∼50 pc at a distance of ∼ 8 kpc, respectively (Reid et al. 2014; Gravity Collaboration 2018).

stellar systems (e.g. Oey 1996a,b; Pellegrini, Baldwin & Ferland 2010, 2011). More recent efforts have focused on measuring and comparing the internal pressure components from different feedback mechanisms in H II regions located within the Small and Large Magellanic Clouds (SMC and LMC, respectively), such as the well-known 30 Doradus complex (e.g. Lopez et al. 2011, 2014; Chevance et al. 2016; McLeod et al. 2019), as well as other nearby galaxies (e.g. McLeod et al. 2020). These studies have provided important insights into early-stage feedback, but further work is needed to understand how pre-processing varies with environment, particularly to higher density, pressure, and metallicity regimes such as those in galactic nuclei and high-redshift galaxies.

Most of the literature to date naturally focuses on regions that are observationally accessible in the local Universe, which are characterized by low gas pressures ($P/k \sim 10^{4-5}$ K cm^{-3}). The ambient gas pressure plays a major role in the molecular cloud lifecycle (Chevance et al. 2020b), specifically by setting the initial conditions for star formation (e.g. Faesi, Lada & Forbrich 2018; Sun et al. 2018, 2020; Jeffreson et al. 2020), the subsequent star formation efficiency (e.g. Krumholz & McKee 2005; Blitz & Rosolowsky 2006; Federrath & Klessen 2012), and the impact of stellar feedback (e.g. Grudić et al. 2018; Kim, Kim & Ostriker 2018; Fujimoto et al. 2019; Li et al. 2019; Keller et al. 2020). This is particularly important, because ISM pressures observed at the peak of the cosmic star formation history are several orders of magnitude higher than those observed in disc galaxies today (e.g. Genzel et al. 2011; Swinbank et al. 2011, 2012; Tacconi et al. 2013). It is therefore a critical question how the physics of star formation and feedback proceeded under the extreme pressures observed at the time that the Universe was forming stars most rapidly. In this work, we investigate the effect of higher ambient density and pressure host environments on the physical properties and evolution of pre-SNe high-mass star formation regions. For this, we focus on the inner few hundred parsecs of the Milky Way, known as the 'Central Molecular Zone' (CMZ; e.g. Morris & Serabyn 1996), which is known to host several (pre-SNe) H II region complexes (e.g. Mehringer et al. 1992; Schmiedeke et al. 2016; Anderson et al. 2020). This region has average gas densities, gas temperatures, ambient pressures, turbulent velocity dispersions, interstellar radiation fields, and cosmic ray ionization rates factors of a few to several orders of magnitude larger than observed in typical Milky Way disc and SMC/LMC star-forming systems, more similar to starburst and high-redshift galaxies at the epoch of peak star formation density at $z \sim 1-3$ (Kruijssen & Longmore 2013). Fig. 1 presents a three-colour image of the Galactic

Table 1. The global properties of the Galactic Centre molecular clouds and H II regions (Barnes et al. 2017, Tables 4 and 5). The columns list the effective radii, molecular gas masses, total embedded stellar mass, the times since pericentre passage (i.e. point of triggered molecular clouds collapse) as estimated from the orbital model of Kruijssen et al. (2015), and the age of the H II regions defined as $t_{\rm p,\,last} - t_{\rm p,\,last}$(dust-ridge) (Section 3.2). In this work, we make the assumption that the dust-ridge molecular clouds represent the precursors to the identified H II regions (see Fig. 1).

Source	$R_{\rm eff}$ (pc)	$M_{\rm gas}$ (10^4 M$_\odot$)	M_* (10^3 M$_\odot$)	$t_{\rm p,\,last}$ (Myr)	$t_{\rm age}$ (Myr)
Dust-ridge*	1.6	3.7	<0.1	<0.53	0
Sgr B2	2.7	65	33	0.74	0.21
G0.6	2.8	4.6	3.3	1.45	0.92
Sgr B1	5.8	8.7	8.0	1.55	1.02
G0.3	6.5	9.3	6.2	1.75	1.22

*Note.**Shown is the average radius, gas mass, and stellar mass of the 'Brick', 'b', 'c', 'd', 'e', and 'f' molecular clouds on the dust-ridge (Barnes et al. 2017).

Centre with the CMZ region highlighted by the white rectangle, and several sources of interest within the regions labelled, such as the Arches and Quintuplet young massive clusters (e.g. Espinoza et al. 2009; Harfst et al. 2010) and the central supermassive black hole (Sgr A*; e.g. Gravity Collaboration 2018). The inset image shows a zoom-in of the so-called 'ionized ridge' region of the CMZ that contains the H II regions complexes we study this work: Sgr B2, G0.6, Sgr B1, and G0.3. We also highlight the quiescent precursor molecular clouds on the 'dust-ridge' (e.g. Lis et al. 1994; Longmore et al. 2012, 2013a; Walker et al. 2015, 2016, 2018; Barnes et al. 2019; Henshaw et al. 2019; Battersby et al. 2020). This dust-ridge is thought to be connected to the ionized ridge via a ring of material surrounding the Galactic Centre found in simulations (e.g. Sormani et al. 2018; Dale, Kruijssen & Longmore 2019; Kruijssen et al. 2019a; Sormani et al. 2020; Tress et al. 2020) and extragalactic systems (e.g. Comerón et al. 2010; Krieger et al. 2020), which is maintained by the inflow of material from the bar (e.g. Krumholz & Kruijssen 2015; Henshaw, Longmore & Kruijssen 2016b; Sormani & Barnes 2019). On the Fig. 1 inset, we also show age estimates of the H II regions based on the predictions from an orbital model (increasing age from left to right; Longmore et al. 2013b; Kruijssen et al. 2015). We summarize the physical properties of the precursor molecular clouds and the H II regions in Table 1 (adopted from Barnes et al. 2017). This paper is organized as follows. In Section 2 we outline how we determine each of the internal pressure components of the Galactic Centre H II regions. In Section 3 we analyse the radial dependence of these pressure components and estimate the energies and momenta of the expanding H II regions. In Section 4 we discuss our findings in the context of the previous observations of the SMC and LMC, compared to analytic models for the expansion of H II regions, and explore how efficiently the stellar population is driving the expansion. Finally, we summarize the results in Section 5.

2 PRESSURE CALCULATION

2.1 Internal H II region pressure components

The internal pressure within an H II region produced by an embedded stellar population can be expressed as the sum of four dominant pressure components (e.g. Lopez et al. 2011, 2014; McLeod et al. 2019):

I) warm ionized thermal gas pressure,
II) direct radiation pressure,
III) dust processed radiation pressure,
IV) hot X-ray emitting thermal gas pressure,

such that the total internal pressure is,

$$P_{\rm tot} = P_{\rm HII} + P_{\rm dir} + P_{\rm IR} + P_{\rm X}. \quad (1)$$

In this section, we discuss the methodology used to determine the $P_{\rm H\,II}$, $P_{\rm dir}$, and $P_{\rm IR}$ pressure components within the Galactic Centre H II regions. We mention $P_{\rm X}$ here because it is included in the comparison to the LMC and SMC (Section 4.1; Lopez et al. 2011, 2014). Lopez et al. determine $P_{\rm X}$ by modelling the thermal (free–free) emission from the hot gas, which peaks at soft X-ray energies for temperatures of $T_{\rm x} \sim 10^6$ K ($k_{\rm B}T_{\rm x} \sim 0.1$ keV). Unfortunately, we cannot make a similar measurement for the Galactic Centre region, for two reasons. First, the Galactic Centre hosts significant non-thermal soft X-ray emission that is expected to be significantly brighter than any potential thermal emission (e.g. Law & Yusef-Zadeh 2005; Yusef-Zadeh et al. 2007; Nobukawa et al. 2008; Ponti et al. 2015; Zhang et al. 2015). Secondly, the substantial column density of foreground material towards the Galactic Centre H II regions is expected to make any thermal soft X-ray emission undetectable. For example, the average molecular hydrogen column density for the H II regions is $\sim 3 \times 10^{22}$ cm^{-2}, which when using the dust grain models from Draine (2003) corresponds to a line-of-sight extinction of $A_{\rm 100eV} > 20$ mag.[1] Such a high X-ray extinction would cause even the most luminous known H II regions to become undetectable for any plausible amount of e.g. *Chandra* observing time. We, therefore, omit the determination of $P_{\rm X}$ within the Galactic Centre from our analysis.

2.1.1 P_{HII}: Thermal pressure from warm (10^4 K) ionized gas

H II regions are ionized by the large flux of H-ionizing Lyman continuum, $\mathcal{N}_{\rm LyC}$, produced by young high-mass stars (>8 M$_\odot$). This pressure in this ionized gas is set by the ideal gas law, $P_{\rm HII} = 2\,n_{\rm e}k_{\rm B}\,T_{\rm HII}$, where the factor of two comes from the assumption that all the He is singly ionized (i.e. $n_{\rm e} + n_{\rm H} + n_{\rm He} = 2n_{\rm e}$). Free–free interactions between the electrons and ions give rise to continuum emission at cm-(mm) wavelengths. The intensity and physical size of this emission can be used to derive the electron density of the ionized gas. Lopez et al. (2011, 2014) determine the electron density for the LMC and SMC sources from their radio continuum fluxes using the expression given by Rybicki & Lightman (1979). However, we choose to use the conversion presented by Mezger & Henderson (1967), as this was adopted by the most comprehensive survey of (ultracompact) H II regions within the Galactic Centre sample by Schmiedeke et al. (2016). The difference in derived electron density using the two methods is only of order 25 per cent, so does not affect the conclusions drawn from the data.[2] The Mezger & Henderson

[1]Using $A_\lambda = (2.5/\ln 10)C_{\rm ext}(\lambda)\,N_{\rm H} = 1.086C_{\rm ext}(\lambda)\,N_{\rm H}$, and the extinction cross-section per H nucleon, $C_{\rm ext}(\lambda)$, at 100 eV of $C_{\rm ext}(0.0124\,\mu{\rm m}) = 7.238 \times 10^{-22}$ cm^2 (see Table 6 of Draine 2003).

[2]This comparison was made for a 1 Jy source at 5 GHz, with a radius of 1 arcsec at 8 kpc. For this calculation, we use equation (5.14b) from Rybicki & Lightman (1979), rather than Lopez et al. (2011, equation 6) and Lopez et al. (2014, equation 10), which have an incorrect constant of 6.8×10^{38} cm^{-3} erg^{-1} K$^{-0.5}$. Rearranging equation (5.14b) from Rybicki & Lightman (1979), we find a constant of 1.46×10^{37} cm^{-3} erg^{-1} K$^{-0.5}$.

Table 2. The sample of radio observations taken from the literature that have been used to calculate the warm ionized gas pressure. We list the telescope, the frequency, and reference for each observation.

ID	Telescope	Frequency (GHz)	References
1	Pencil-beam antenna (Single dish)	2 & 4 & 6 & 10	Downes & Maxwell (1966)
2	NRAO's 36-foot reflector (Single dish)	31	Downes, Maxwell & Rinehart (1970)
3	Naval Research Laboratory's 85-foot reflector (Single dish)	11 & 18 & 32	Hobbs & Johnston (1971)
4	NRAO's 36-foot reflector (Single dish)	85	Hobbs, Modali & Maran (1971)
5	Wilkinson Microwave Anisotropy Probe (WMAP; Single dish)	93	Lee, Murray & Rahman (2012)
6	Molonglo Observatory Synthesis Telescope (MOST; Interferometer)	0.4	Little (1974)
7	Very Large Array (VLA; Interferometer)	5 & 15	Benson & Johnston (1984)
8	Very Large Array (VLA; Interferometer)	15	Roelfsema et al. (1987)
9	Very Large Array (VLA; Interferometer)	15	Gaume & Claussen (1990)
10	Very Large Array (VLA; Interferometer)	1.5 & 5 & 8	Mehringer et al. (1992)
11	Very Large Array (VLA; Interferometer)	0.3	Yusef-Zadeh et al. (2007)
12	Very Large Array (VLA; Interferometer)	23 & 43	Schmiedeke et al. (2016)

(1967) conversion can be given as,

$$n_{\rm e} = 2.576 \times 10^6 \left(\frac{F_\nu}{\rm Jy}\right)^{0.5} \left(\frac{T_{\rm HII}}{\rm K}\right)^{0.175} \left(\frac{\nu}{\rm GHz}\right)^{0.05} \times \left(\frac{\theta_{\rm source}}{\rm arcsec}\right)^{-1.5} \left(\frac{D}{\rm pc}\right)^{-0.5} {\rm cm}^{-3}, \quad (2)$$

where F_ν is the measured flux, ν is the frequency of the observations, $T_{\rm H\,II}$ is the electron temperature, D is the source distance, and $\theta_{\rm source}$ is the circular diameter of the source. Observations of the Galactic Centre at radio wavelengths have been possible for several decades, hence there is an extensive library of data taken at various frequencies and resolutions. We choose a sample of observations from both single-dish and interferometer telescopes, which are listed in Table 2, along with the frequencies and reference for each observation. To calculate $n_{\rm e}$ for each of the literature catalogue flux and diameters, we assume a source distance of 8 kpc (e.g. Reid et al. 2016), and $T_{\rm H\,II} = 5000$ K. These values of $n_{\rm e}$ are then used with $T_{\rm H\,II}$ to determine $P_{\rm H\,II}$. The low $T_{\rm H\,II}$ used in the above calculation has been chosen to account for the well-studied systematic decrease of $T_{\rm H\,II}$ observed at decreasing galactocentric radius, caused by the corresponding increase in metallicity; the typical electron temperature at solar metallicity is ~ 7000 K (e.g. Mezger et al. 1979; Shaver et al. 1983; Wink, Wilson & Bieging 1983; Caswell & Haynes 1987; Deharveng et al. 2000; Giveon et al. 2002). When extrapolating the electron temperature to galactocentric radius relation from Deharveng et al. (2000) down to $R_{\rm GC} = 0$ kpc, we find $T_{\rm H\,II} = 4260 \pm 350$ K. This result is in agreement with the median $T_{\rm H\,II} \sim 5000$ K measured across a several Galactic Centre H II regions (Gaume & Claussen 1990; Mehringer et al. 1992; Cram et al. 1996; Lang, Goss & Wood 1997; Lang, Goss & Morris 2001). Therefore, we adopt $T_{\rm H\,II} = 5000$ K as the representative value for Galactic Centre H II regions, and use this electron temperature for all calculations within this work.

2.1.2 $P_{\rm dir}$: *Direct radiation pressure*

The large radiation field directly produced from young stellar objects can exert a significant pressure on the surrounding material. This radiation pressure, $P_{\rm rad}$, at a given position within an H II region, is related to the bolometric luminosity, $L_{\rm bol}$, of the stellar population and the distance, r, from each star to that position within the region:

$$P_{\rm rad} = \sum \frac{L_{\rm bol}}{4\pi r^2 c}, \quad (3)$$

where the summation is over all stars within the region. The volume-averaged direct radiation pressure, $P_{\rm dir}$, is then given as (Lopez et al. 2014),

$$P_{\rm dir} = \frac{3L_{\rm bol}}{4\pi R^2 c}, \quad (4)$$

where R is the radius of the H II region (or effective radius, $R_{\rm eff}$, that we define later and use throughout the rest of the paper), and $L_{\rm bol}$ is the bolometric luminosity from the population of massive stars within the H II region. This form differs by a factor of three from McLeod et al. (2019, equation 4), as these authors calculate the radiation surface pressure rather than the volume average pressure. This expression is appropriate to compute the force balance at the surface of an empty shell. However, as this work aims at understanding the large-scale dynamics of the Galactic Centre H II regions (e.g. the total energy and pressure budget for each source), the inclusion of a factor of three in the numerator of the above equation is required. We also note here that the higher metallicity within the Galactic Centre, or increasing the amount of dust, has no effect on the $P_{\rm dir}$ calculation. Direct radiation pressure is limited by the momentum supplied by the stellar radiation field, and, as long as there is enough dust around to absorb all the radiation, the momentum per unit time delivered is the same. Lopez et al. (2011) determine the bolometric luminosity of the H II regions within the LMC and SMC from Hα emission. However, this is not possible for the H II regions investigated here, due to the high optical extinction towards the Galactic Centre ($A_{\rm v} > 20$ mag), which completely obscures any Hα emission. We, therefore, adopt two alternative methods of calculating the bolometric luminosity using radio and infrared observations (i.e. wavelengths where the emission is much less affected by dust extinction). First, we can make the assumption that the bolometric luminosity is proportional to the flux of ionizing photons, $\mathcal{N}_{\rm LyC}$, such that $L_{\rm bol} = \mathcal{N}_{\rm LyC} \langle h\nu \rangle$, where $\langle h\nu \rangle \sim 15$ eV is the mean photon energy (Pellegrini et al. 2007). We use the $\mathcal{N}_{\rm LyC}$ for each H II region as determined from the radio observations outlined in Table 2 (i.e. Gaume & Claussen 1990; Mehringer et al. 1992; Schmiedeke et al. 2016), and solve for the direct radiation pressure using equation (4). The second method assumes that the luminosity integrated over infrared wavelengths approximately corresponds to the total bolometric luminosity. This is a common assumption made for embedded star-forming regions, where the luminosity from massive stars produced at ultraviolet wavelengths is absorbed and remitted by the dust in the infrared. Barnes et al. (2017) have produced maps of the total infrared luminosity across the Galactic Centre. These authors fit a two-component modified blackbody function to extinction corrected

5.8–24 μm (Carey et al. 2009; Churchwell et al. 2009) and 160–500 μm (Molinari et al. 2010) emission maps (referred to as the warm and cool component of the bolometric luminosity; see fig. 2 of Barnes et al. 2017). These infrared (i.e. bolometric) luminosity maps are used with the two methods outlined below to also determine the direct radiation pressure within each of the Galactic Centre H II regions. In comparison with the first method for calculating the direct radiation pressure from radio observations, we choose to identify individual sources within the infrared maps. These can be considered as discrete H II regions each with a single value of the direct radiation pressure. We choose to identify these H II regions in the map of the warm component of the bolometric luminosity using a dendrogram analysis (Rosolowsky et al. 2008). We choose to use a structure finding algorithm, as opposed to by-eye identification, to give reproducibility within regions with particularly complex morphology (the warm bolometric luminosity map is given in fig. 2 from Barnes et al. 2017).[3] We make use of the 'leaves' identified from the dendrogram analysis, which are the highest level (i.e. smallest) structures in the analysis and here represent distinct H II regions. We take the mask of each H II regions (dendrogram leaf), and apply this to both the warm and cool bolometric luminosity component maps, which we sum to then get the total bolometric luminosity. This is used with equation (4) to get the direct radiation pressure ($P_{\rm dir}$) within each H II region. The effective radius ($R_{\rm eff}$) of each H II region is defined as the radius for a circle with the corresponding area (A) of each structure (i.e. $R_{\rm eff} = \sqrt{A/\pi}$). In addition to the dendrogram analysis, we also calculate the direct radiation pressure within apertures of increasing radius from the centre of each H II region complex. To do so, we place circular masks for each source on to both the warm and cool bolometric luminosity component maps, and sum the enclosed values to then get the total bolometric luminosity. The circle is then increased in radius, and the process repeated. We again use equation (4) to determine the direct radiation pressure within these increasing circular apertures. This method differs from the dendrogram analysis, as it returns a continuous radial distribution from the source centre, as opposed to a distribution of distinct H II region with various sizes.

2.1.3 P_{IR}: Dust-processed radiation pressure

The luminosity from the young massive stars peaks at ultraviolet wavelengths. However, this regime is completely obscured for most embedded star-forming regions. Rather, the ultraviolet emission from the majority of young stars is absorbed by the surrounding dust from the host molecular cloud. This then heats the dust from tens to hundreds of Kelvin, so that it emits predominantly at infrared wavelengths. The radiation field produced by the heated dust then provides an expansion pressure, which can be given as,

$$P_{\rm IR} = \frac{1}{3}u, \tag{5}$$

where u is the radiation field absorbed by the dust. To estimate u, we compare the observed 5.8, 8, 24, and 70 μm (Carey et al. 2009; Churchwell et al. 2009; Molinari et al. 2010) infrared flux densities to those predicted for the dust models of Draine & Li (2007). These dust models produce synthetic spectral energy distributions for a range of radiation fields and dust compositions. The latter is parametrized by the fraction of dust in polycyclic aromatic hydrocarbons, $q_{\rm PAH}$, which produce substantial emission at the observed infrared wavelengths. The former is parametrized by the dimensionless scale factor of the radiation absorbed by the dust, U, which measures the radiation field energy density normalized to the local interstellar radiation field (ISRF) energy density,

$$u = U u^{\rm ISRF}. \tag{6}$$

Here, $u^{\rm ISRF} = 8.65 \times 10^{-13}\,{\rm erg\,cm^{-3}}$ is the energy density of non-ionizing photons in the local interstellar medium. To compare the observed 5.8, 8, 24, and 70 μm infrared flux densities for the H II regions to those predicted by the dust models, we smooth the infrared maps to a common resolution of 11.5 arcsec. Following Barnes et al. (2017), we then use the prescriptions of Cardelli, Clayton & Mathis (1989) and Chapman et al. (2009) to correct the 5.8, 8, and 24 μm fluxes for a constant visual extinction of $A_{\rm v} = 20$ mag, which is typical for lines of sight towards the Galactic Centre (Figer et al. 1999; Dutra et al. 2003; Schödel et al. 2010). Additionally, we determine the extinction along each line of sight using the molecular hydrogen column density map (e.g. Molinari et al. 2011; Battersby et al., in preparation). To do so, we use the conversion from column density to visual extinction from Fitzpatrick (1999), and then the conversions from visual to infrared extinction from Cardelli et al. (1989) and Chapman et al. (2009). When doing so we find that Sgr B2 has a very high infrared extinction for the majority of its sight-lines ($A_{8\mu{\rm m}} > 10$ mag, equal to a visual extinction of $A_{\rm v} > 100$ mag), which cannot be accurately corrected. It has, therefore, been omitted from this analysis of the dust-processed radiation pressure. We remove the contribution of star-light from the 8 and 24 μm flux density maps using the 3.6μm flux density map with (Lopez et al. 2011, 2014),

$$F_8^{\rm ns} = F_8 - 0.232F_{3.6} \;\text{ and }\; F_{24}^{\rm ns} = F_{24} - 0.032F_{3.6}, \tag{7}$$

where the subscript denotes the wavelength, and superscript denotes the non-stellar flux densities. Due to the very small 3.6 μm flux density observed within the Galactic Centre, this subtraction has a minimal effect. Ratios of the observed 8, 24, and 70 μm fluxes ($F_8^{\rm ns}$, $F_{24}^{\rm ns}$, and F_{70}) are required to compare to the Draine & Li (2007) dust models. These ratios for all the pixels within each of the Galactic Centre H II regions are shown in the upper panel of Fig. 2. We overplot on the measurements a grid of flux ratios predicted from the dust model. When corrected for a constant extinction, we find that G0.6, Sgr B1, and G0.3 have flux ratios well covered by the dust model grid. However, when we correct for the extinction along each line of sight using the column density measurements, several of the flux ratio values fall out of the dust model grid parameter space (e.g. to the right of the grid plotted in the upper panel of Fig. 2). We note that we are interested in the value of the radiation absorbed by the dust to calculate the dust processed radiation pressure, and the values of U are close to constant for a given $F_{24}^{\rm ns}/F_{70}$ (i.e. horizontal grid lines). Therefore, we interpolate the U value for the observed $F_{24}^{\rm ns}/F_{70}$ from the dust model grid for any values that fall out of the grid parameter space; i.e. ignoring any $F_8^{\rm ns}/F_{24}^{\rm ns}$ dependence. We use the interpolate.griddata[4] of SCIPY package in IPYTHON to interpolate the grid of predicted flux ratios from the dust models on to the observed values. The lower panel of Fig. 2 shows the values of U as a function

[3]The following set of parameters are used for determination of the dendrogram structure: min_value $= 3\,\sigma \sim 300\,{\rm L}_\odot$ (the minimum luminosity considered in the analysis); min_delta $= 3\,\sigma$ (the minimum spacing between isocontours); min_delta $= 1/3$ beam ~ 3 pixels (the minimum number of pixels contained within a structure). Varying the dendrogram parameters over a wide range of values does not affect the results of the paper.

[4]http://docs.scipy.org

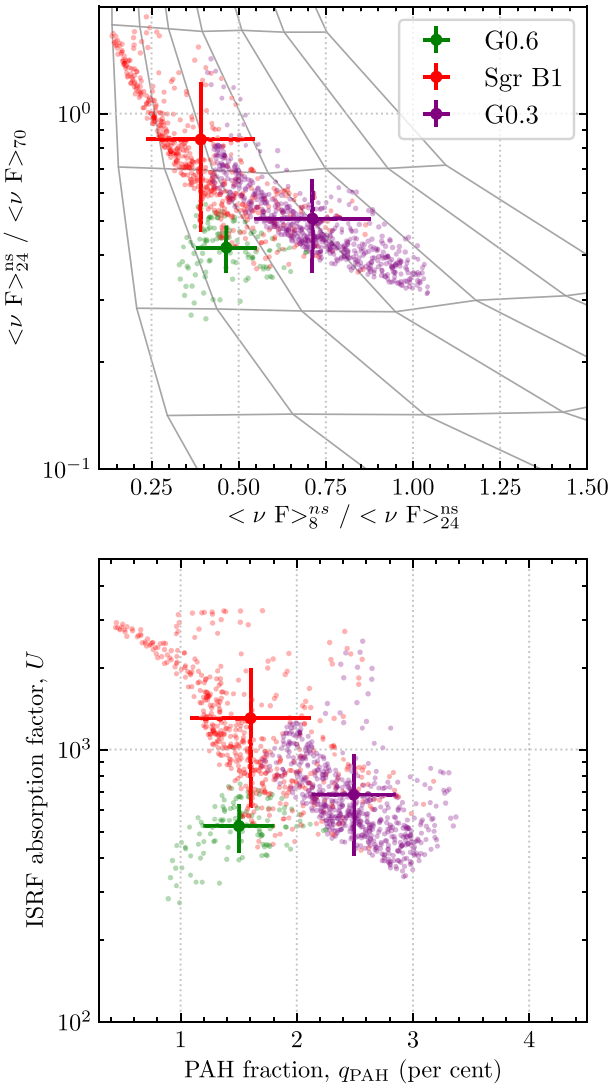

Figure 2. Dust properties used to calculate the pressure component from the dust reprocessed emission. The upper panel shows the extinction and star-light contribution corrected infrared flux ratios for all pixels within each (proto)-cluster. We overplot a grid of the predicted flux density ratio from the dust model for various values of the fraction of dust in polycyclic aromatic hydrocarbons, q_{PAH}, and the dimensionless scale factor of the radiation absorbed by the dust, U. Horizontal lines show q_{PAH} = 0.47, 1.12, 1.77, 2.50, 3.19, 3.90, 4.58 from left to right, and vertical lines show U = 5, 15, 25, 100, 300, 1000, and 3000 from bottom to top. The lower panel shows the results from the interpolation of the q_{PAH} and U dust model grid on to the observed flux ratios. The 5.8, 8, and 24 μm fluxes have been corrected for a constant visual extinction of $A_{\mathrm{v}} = 20$ mag (Figer, McLean & Morris 1999; Dutra et al. 2003; Schödel et al. 2010). Sgr B2 has been omitted from this analysis due to the high infrared extinction ($A_{8\mu\mathrm{m}} > 10$ mag, equal to a visual extinction of $A_{\mathrm{v}} > 100$ mag).

of q_{PAH} for all pixels from this interpolation process (for a constant extinction correction). The values of U determined using a constant and varying extinction are used in equation (6) to determine the dust processed pressure component. It is worth briefly mentioning here that by using the dust model to get q_{PAH}, we are effectively accounting for the high Galactic Centre metallicity when determining U and, hence, P_{IR}. The absolute metallicity or dust abundance does not matter very much for the Draine & Li (2007) models we are adopting. This is because the modelling we conduct here amounts to asking what spectrum the dust will emit, assuming it is exposed to a certain background radiation field and that the optical depth to the re-emitted infrared is small. Since only the spectral shape is being used in the calculation, doubling the number of grains per unit volume has no effect, since it does not change the spectral shape, just the absolute luminosity. There could be a subdominant effect in that the grain size distribution may be different for the Galactic Centre than it is at lower metallicity. This will make a difference, because the spectral energy distribution is sensitive to the grain size distribution. However, there is no evidence that the grain size distribution is significantly different for supersolar metallicity, and, to the extent that it is, the first-order variation is captured by our variation of the PAH fraction (q_{PAH}). Again, as in Section 2.1.2, we adopt the two methods for calculating the pressure as a function of the size scale. First, we take the H II region (i.e. leaf boundary) masks produced from the dendrogram analysis, and apply these to the U maps for each source to get a measure P_{IR} within distinct H II regions of different sizes. Secondly, we calculate the average U within circular apertures of increasing radius, which gives a radial dependence of P_{IR} from the centre of each source.

2.2 Total internal HII region pressure

Using the methods presented in this section, we have calculated the ionized gas ($P_{\mathrm{H\,II}}$), direct radiation (P_{dir}), and dust reprocessed (P_{IR}) pressure components for our sample of Galactic Centre H II regions. Fig. 3 shows how these various pressure components vary as a function of the size scale for each of the Galactic Centre sources. The direct radiation pressure is shown by the blue lines and points, the warm ionized gas pressure is shown by the red points, and the dust reprocessed emission pressure is shown by the purple lines and points. The numbers within the legend correspond to the references provided within Table 2. On the smallest scales ($\sim 10^{-3}$ pc), the direct radiation pressure is factors of several higher than the ionized gas thermal pressure. However, we find that the direct radiation pressure decreases steeply with increasing radius (see dotted lines overlaid on each panel), and on scales of $\sim 10^{-2}$ pc both the direct and ionized gas pressure components are equal within the observed scatter. On intermediate scales (0.01–0.1 pc; Sg B2, G0.6, Sgr B1), we find that the direct radiation and ionized thermal pressure components remain approximately equal within around an order of magnitude scatter. On the large scale (> 0.1–20 pc), we find that the direct radiation is typically less than both the ionized thermal pressure gas and the dust-processed pressures, which are comparable. Where measurements are available for all three of the pressure components on the largest scales (G0.6 and Sgr B1), we find that the ionized thermal pressure component is the dominant pressure term driving the H II region expansion. It is worth considering at this stage how the radial trends displayed in Fig. 3 should be interpreted. First, the P_{dir} and $P_{\mathrm{H\,II}}$ points have been calculated in two ways: one method using radio observations, and another method using IR observations. The former provides measurements of the same H II regions at different spatial resolutions. The latter uses dendrograms to identify distinct H II regions, each of which can have a different physical size depending on the dendrogram analysis. Therefore, increasing in radius in Fig. 3 can mean that either (i) distinct increasingly larger H II regions have been identified within each source, or (ii) these larger radii data points are larger aperture averages of the smaller effective radii H II regions that they contain. The fact that the radial trend is the same for both methods using two different, widely separated wavelength observations show the results are robust

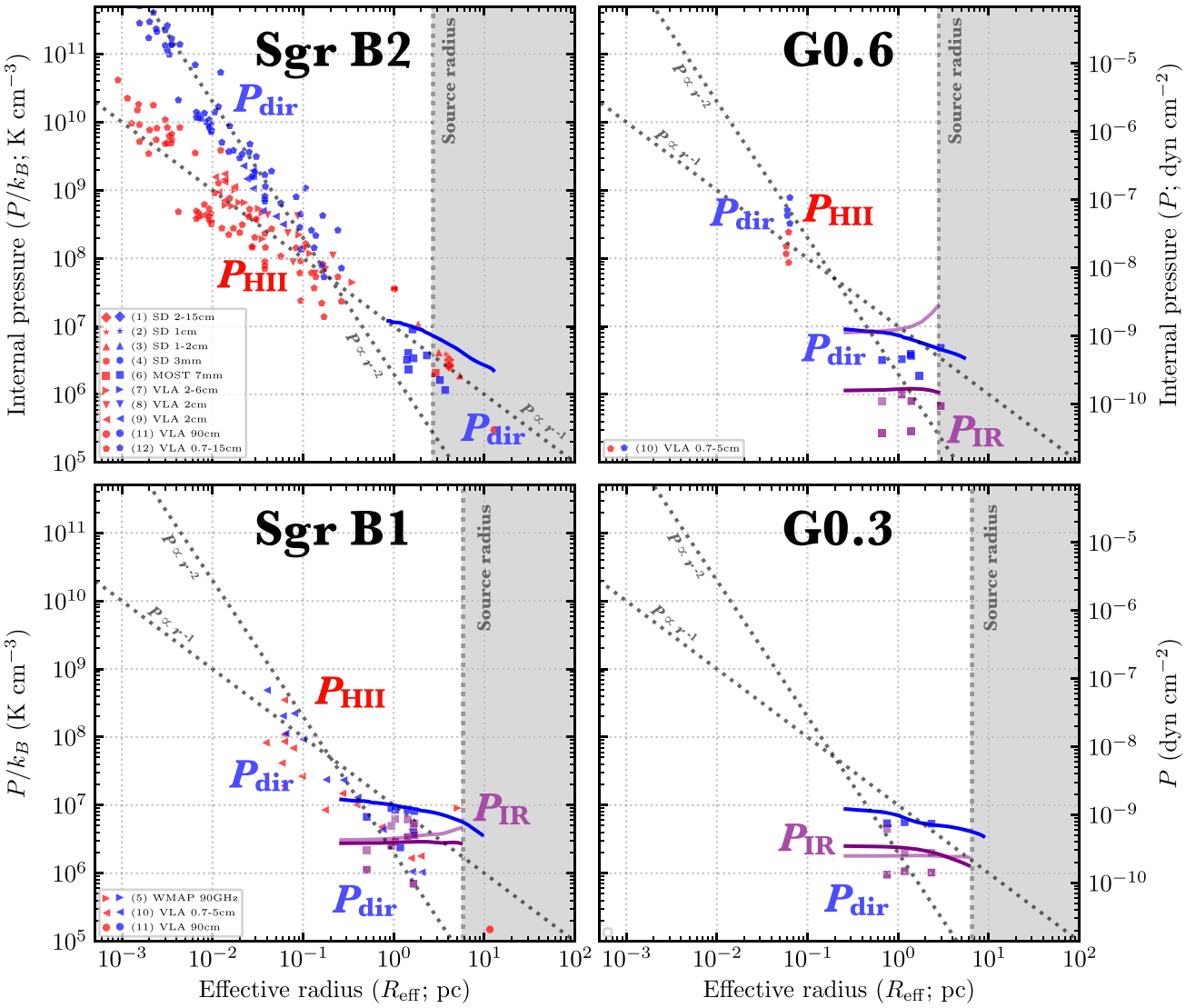

Figure 3. The pressure as a function of effective radius for each source. The points within this plot represent discrete measurements of the pressure calculated from sources identified from various resolution radio data sets that have been taken from the literature (see Table 2), or from the sources identified within the available infrared observations (see Sections 2.1.2 and 2.1.3). The lines represent radial profiles from the centre of each source, which have been determined using the infrared observations (Sections 2.1.2 and 2.1.3). The blue points and lines show the direct radiation pressure ($P_{\rm dir}$; Section 2.1.2), purple points and lines show the dust reprocessed emission pressure ($P_{\rm IR}$; Section 2.1.3), red points indicate the warm ionized gas pressure ($P_{\rm H\,II}$; Section 2.1.1). The faded purple lines and points show the result of using the extinction determined along each line of sight, as opposed to using a constant value, for the $P_{\rm IR}$ analysis (see Section 2.1.3). The legend shows the references for the radio data used to determine these pressure components, where the numbers correspond to the reference IDs provided in Table 2. We overlaid diagonal lines corresponding to $P \propto r^{-1}$ and $P \propto r^{-2}$ for reference. The vertical black dashed line is the measured effective radius for each source (see Table 1). Points within the shaded grey region are larger than the measured source sizes, and, therefore, may have spatial overlap with adjacent sources (see source ellipses shown in Fig. 1). Analysis within the shaded portion of the parameter space should be treated with caution. The discrete measurements of each pressure component, shown as points within this plot, are given in Table A1 and a machine-readable table in the online supplementary material of this work.

against the choice of method. We conclude that a simplistic but reasonable interpretation of the points plotted within Fig. 3 are that they represent pressure components as a function of H II region size. This is subtly different from the lines plotted in Fig. 3, which have been determined from increasing size apertures from the centre of each H II region. The lines then represent a radial dependence of the pressure components. In the interest of a comparison, both of the methods have been plotted on Fig. 3, yet caution should be taken in drawing conclusions based on both the radial (lines) and size (points) distributions.

3 PRESSURE PROFILES AND FEEDBACK-DRIVEN DYNAMICS

3.1 Pressure components as radially decreasing power laws

To examine how the pressure components determined in Section 2 scale with effective radius (size), we perform a power-law fit to the points shown in Fig. 3. We fit a power-law relation of $P = a(R_{\rm eff}/{\rm pc})^{-b}$ to each of the pressure components, using the numpy.polyfit least-squares fitting routine in log–log space. This analysis is limited to

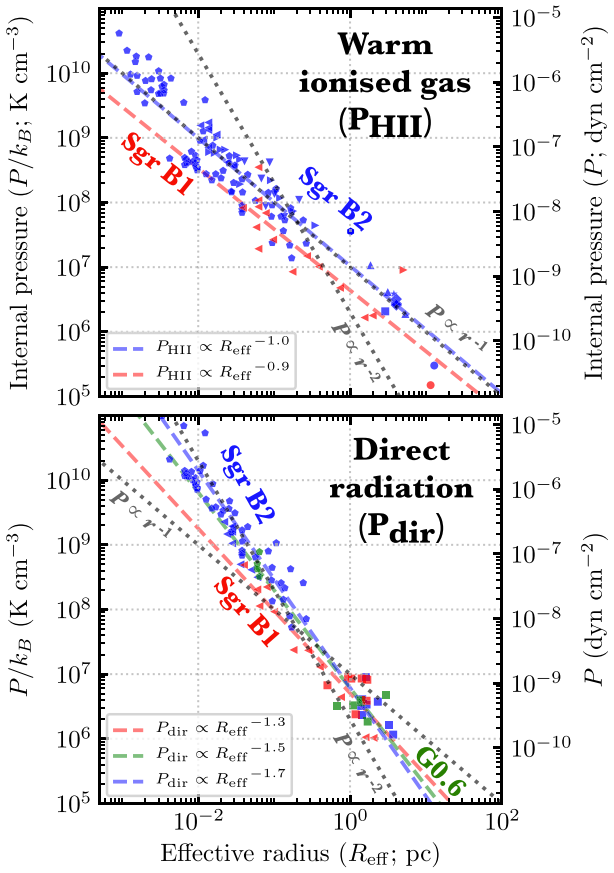

Figure 4. The observed pressure as a function of radius for each source (labelled at the top of each panel). The symbols for each observed component are identical to those shown in Fig. 3. Shown as diagonal dashed lines are the power-law fits to the pressure components for each source. The parameters of these fits are given in the legend of each panel, and are summarized in Table 3. The diagonal grey dotten line shows $P \propto r^{-1}$ and $P \propto r^{-2}$ for reference.

Table 3. The pressure components as a function of radius power-law fit parameters as shown in Fig. 4. These have been determined using a least-squares fitting routine in log–log space for $P = a(R_{eff}/pc)^{-b}$, where a and b are tabulated as the constant and power in this table (see Section 3.1). This analysis has been limited to the warm ionized gas pressure and direct radiation pressure, and for sources that have pressure components determined over a sufficient range in effective radius to allow for statistically significant power-law fits.

Pressure	Sources	Power; b	Constant; log(a) (K cm^{-3})
P_{HII}	Sgr B2	-0.99 ± 0.03	7.02 ± 0.06
P_{HII}	Sgr B1	-0.94 ± 0.14	6.64 ± 0.13
P_{dir}	Sgr B2	-1.68 ± 0.04	6.79 ± 0.07
P_{dir}	G0.6	-1.51 ± 0.15	6.78 ± 0.12
P_{dir}	Sgr B1	-1.27 ± 0.1	6.71 ± 0.08

the warm ionized gas pressure and direct radiation pressure, and for sources which have pressure components determined over a sufficient range in effective radius to allow for statistically significant power-law fits. Fig. 4 displays the observed pressure components overlaid with the results of the fitting routine (as labelled). The parameters of each fit are given in Table 3. We find that the thermal pressure of the ionized gas (P_{HII}) within the Sgr B2 and Sgr B1 sources are both best fit with the relation $P_{H\,II} \propto r^{-1}$. We compare this to what is expected from simple analytic arguments. The ideal gas equation is given as $P_{therm} \propto nT$, where n is the number density, and T is the temperature. The Stromgren radius of an H II region can be expressed as $r^3 \propto \mathcal{N}_{LyC} n^{-2}$, where $\mathcal{N}_{LyC}$ is the flux of ionizing photons (see equation 12; Strömgren 1939). Therefore, we would expect $P_{therm} \propto r^{-3/2}$. We then find that the observed ionized gas pressure decreases less steeply with radius than estimated from these simple thermal pressure arguments (see Section 4.3 for further discussion). We find the direct radiation pressure has a significantly steeper radial trend ($P_{dir} \propto R_{eff}^{-1.5}$) compared to the ionized gas pressure ($P_{HII} \propto R_{eff}^{-1}$). Moreover, we find that there is moderate (± 0.2 in the exponent of the power-law slopes) source-to-source variation for the direct radiation pressure radial relations, which is not observed for the ionized gas pressure. Comparing to this variation to the ages of the H II regions, we infer that the slope of the direct radiation pressure becomes shallower with age (compare Tables 1 and 3).

3.2 Determining the expansion velocity, momentum, and energy of the H II regions

We now want to measure the expansion velocity of the H II regions and the associated energy and momentum required to drive the H II region bubbles. To obtain an accurate expansion velocity for the star-forming clouds, we measure both a photometric expansion rate from the *Spitzer* and *Herschel* MIR luminosity maps, and a spectral expansion rate from radio recombination lines (RRLs).[5] These measurements should represent expansion velocities perpendicular to the line-of-sight and along the line-of-sight, respectively.

3.2.1 Photometric velocity

The model of Kruijssen et al. (2015) predicts that the clouds and H II regions with the CMZ may reside along an orbital stream. In this model, star formations began at pericentre passage with the bottom of the Galactic gravitational potential, when compressive tidal forces are strongest (Longmore et al. 2013b; Kruijssen et al. 2019a; Dale, Kruijssen & Longmore 2019). On this orbit is the dust-ridge (shown in Fig. 1), which shows increasing signs of active star formation from the point of pericentre passage. Cloud e/f (see Fig. 1) is the first cloud in this sequence that shows several signs that star formation has recently begun (e.g. maser emission) so we use this as the zero-point for star formation activity. We use the difference in time along the orbit from cloud e/f to each of the ionized ridge sources as an estimate of the expansion time of the H II regions. Referring to the nomenclature in Kruijssen et al. (2015), the age of the H II region is given by $t_{age} = t_{p,last} - t_{p,last}(\text{cloud e/f})$. These ages are given in Table 1, and displayed in the inset of Fig. 1. With these, we can give a photometric estimate of the expanding shell velocity, which is defined as,

$$v_{exp,pho} = \frac{R_{eff}}{t_{age}}. \quad (8)$$

The results of this analysis are displayed in Table 4.

[5]Here we use the standard RRL notation of Hn_α, which corresponds to a downward energy level transitions from principal quantum $n + 1$ to n for hydrogen (e.g. $n = 54 \rightarrow 53$ for hydrogen is H53$_\alpha$).

Table 4. Photometrically (Section 3.2.1) and spectroscopically (Section 3.2.2) determined expansion velocities ($v_{\rm exp}$) for the Galactic Centre H II regions. Also tabulated are the (log) energies, and (log) momenta estimated using the average expansion velocities and mass of each H II region (Section 3.2.3).

Source	$v_{\rm exp,\,pho}$ (km s^{-1})	$v_{\rm exp,\,spec}$ (km s^{-1})	log($E_{\rm exp}$) (J)	log($p_{\rm exp}$) (M$_\odot$ km s^{-1})
Sgr B2	12.8	10.7	41.75	4.69
G0.6	3.0	–	41.48	5.00
Sgr B1	5.6	9.2	42.20	5.33
G0.3	5.2	–	41.92	5.21

3.2.2 *Spectral velocity*

As an independent measure of the expansion velocity along the line of sight, we can also use spectroscopic observations. There have been many surveys that have observed the molecular line emission and studied the dynamics of the cool gas within the Galactic Centre. However, studies of the H II region dynamics, and how these fit into the current scenarios of Galactic Centre kinematics are currently lacking. To investigate the ionized gas within the H II regions, we use H52α, H53α, H61α, and H69α recombination line observations taken with the Mopra telescope (Walsh et al. 2008, 2011; Purcell et al. 2012; Jones et al. 2013). Initial inspection of these observations show that the signal-to-noise ratio towards the H II regions is not sufficient to accurately determine kinematic information. To overcome this, we stack the radio recombination lines from the survey that are close in frequency, and then from these stacked maps choose those which have good signal-to-noise values. The maps towards the ionized ridge that have been integrated between 0 and 100 km s^{-1} are shown in the left-hand panel of Fig. 5. These clearly show a strong detection towards the Sgr B2 and Sgr B1 sources, yet lack emission towards G0.6 and G0.3. We, therefore, only analyse Sgr B2 and Sgr B1 in this section. The spectra taken towards the Sgr B2 and Sgr B1 sources from each of these stacked maps are shown in the right-hand panel of Fig. 5. These stacked spectra have been fit with a Gaussian profile using the PYSPECKIT package in python. This fit is overlaid on each of the spectra shown in Fig. 5, and the measured velocity dispersion, $\sigma_{\rm v}$, is shown in the upper left of each panel. To calculate the expansion velocity of each of the H II regions from their measured velocity dispersion, $\sigma_{\rm v}$, we assume that there are several distinct contributions that combined in quadrature to give the observed Gaussian profile. The first of these is the thermal motions of the ionized gas, $\sigma_{\rm T} \sim \sqrt{2.2\,T_{\rm e} k_{\rm B}/m_{\rm H}\mu_{\rm H}} = 8.05$ km s^{-1}, which assumes a mean atomic weight accounting for helium ($\mu_{\rm H} = 1.41$), a factor of 2.2 that accounts for the number of particles (including electrons) per H nucleus, and the typical Galactic Centre H II region electron temperature of 5000 K (see Section 2.1.1). The second of these contributions is the dynamical motions (e.g. rotation, relative motions) inherited from earlier in their evolution as molecular clouds: $\sigma_{\rm D}$. This is taken as the average dispersion of the 'dust-ridge' of 10.8 km s^{-1} (Henshaw et al. 2016a). Lastly, we subtract the contribution from the velocity resolution $v_{\rm res} \sim 0.2$ km s^{-1}. Finally, following Keto, Zhang & Kurtz (2008, their equation 3), we determine the contribution from pressure broadening, $\sigma_{\rm P}$, assuming a $n_{\rm e} = 10^3$ cm^{-3}, which corresponds to the electron density calculated for around a parsec scale within Sgr B2 and B1 (using equation 2 and the flux density measurement of Downes et al. 1970 and Mehringer et al. 1992). We find that the contribution of $\sigma_{\rm P}$ to $\sigma_{\rm v}$ is <1 per cent for the studied radio recombination lines, and, therefore, $\sigma_{\rm P}$ not considered further. The expansion velocity, $v_{\rm exp,\,spec}$, for each of the H II regions is then calculated as

$$\sigma_{\rm v} = \sqrt{\sigma_{\rm D}^2 + \sigma_{\rm T}^2 + \Delta v_{\rm res}^2 + v_{\rm exp,spec}^2}. \quad (9)$$

The results of this analysis are given in Table 4. On average we find spectroscopic expansion velocities for Sgr B2 and B1 of the order 10 km s^{-1}, and both fall within around 50 per cent of the photometric velocities. Given the assumptions made in the derivations of these values, this represents satisfactory agreement.

3.2.3 *Energy and momentum*

In this section, we have determined the expansion velocity of the H II regions using two independent methods, which gives values of $v_{\rm exp}$ for each of the sources within reasonable agreement. The average of these expansion velocities can now be used to calculate how much energy and momentum from the embedded stellar population is imparted on the surrounding environment. The total energy, $E_{\rm exp}$, and momentum, $p_{\rm exp}$, of the expanding gas can be simply calculated as,

$$E_{\rm exp} = \frac{1}{2} M_{\rm ejct}\, v_{\rm exp}^2$$
$$p_{\rm exp} = M_{\rm ejct}\, v_{\rm exp}, \quad (10)$$

where $M_{\rm ejct}$ is,

$$M_{\rm ejct} = M_{\rm gas}^{\rm init} - M_{*}^{\rm final}, \quad (11)$$

where $M_{\rm gas}^{\rm init}$ is the gas mass of the precursor molecular clouds from which the stellar population formed, and $M_{*}^{\rm final}$ is the final stellar mass of the stellar population. Given gas clouds with properties similar to those currently in the dust ridge are the most likely precursors clouds to the stellar populations driving the H II regions, we use the average mass of the dust ridge clouds as our estimate of $M_{\rm gas}^{\rm init}$ (see Table 1). Here we have implicitly made the assumption that the ejecta mass can be represented by the difference in mass between the average dust ridge cloud and the embedded stellar mass within an H II region. Or in other words, all the initial cloud mass that is not converted to stars, is blown away by the H II region as ejecta. We note that, however, this scenario will not strictly be the case, given that we know there is still some dust continuum emission towards the H II regions. This is particularly relevant for Sgr B2, which is thought to be still heavily embedded within its host cloud (see Fig. 1). In light of this, the values of ejecta mass, energy, and momentum calculated in this section should be viewed as upper limits. The resulting energy and momentum values are shown in Table 4. We discuss these values in Section 4.4.

4 DISCUSSION

4.1 Comparison with lower pressure environments

We now compare the pressure components calculated for the Galactic Centre H II regions to those found in other similar observations in the literature. Currently, however, H II regions within a limited sample of sources have been investigated in a comparable manner (e.g. Lopez et al. 2011, 2014; McLeod et al. 2019, 2020). We make use of the data taken from Lopez et al. (2011) who investigated the pressure components within the massive star-forming region 30 Doradus in the LMC, and Lopez et al. (2014, data taken from their Table 7) who then expanded this study to 32 H II regions with ages of $\sim 3-10$ Myr within both the Small and Large Magellanic Clouds (SMC and LMC, respectively). More recently, McLeod et al. (2019, data are taken from their table 7) have used MUSE integral field data to accurately determine the spectral types and luminosity classes of the stellar

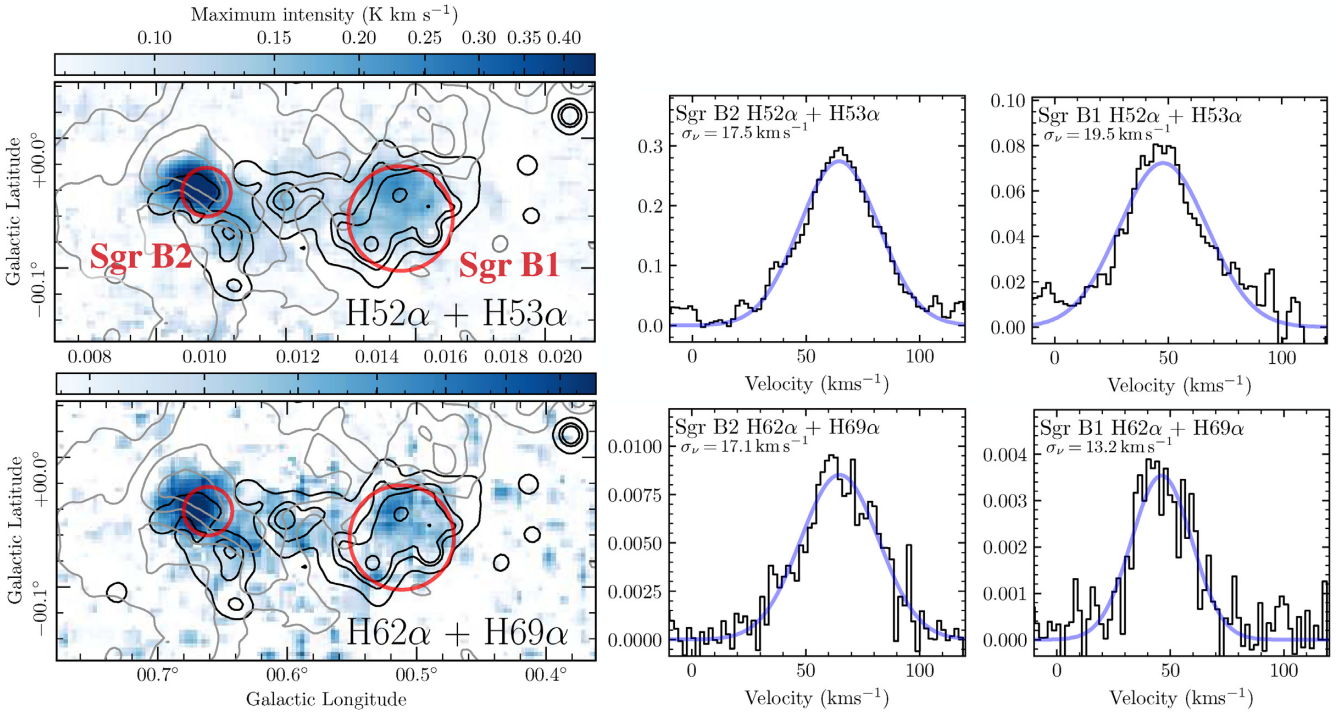

Figure 5. Left-hand panels: The radio recombination lines that have been used to investigate the H II region expansion velocities. These have been taken from the Mopra CMZ survey (Walsh et al. 2008, 2011; Purcell et al. 2012; Jones et al. 2013), and have been smoothed to the same spatial and spectral resolution. To achieve better signal-to-noise, the RRLs with similar frequencies have been stacked (H52 α + H53 α; H61 + H69 α). Right-hand panels: Mean spectra across Sgr B2 and Sgr B1 (Barnes et al. 2017). These have been fit with a single Gaussian velocity component, which is shown as a faded blue curve on each spectrum, and the velocity dispersion from each fit is shown at the top of each panel.

populations within two H II region complexes in the LMC.[6] From this they determine the direct radiation and ionized gas pressure components of the feedback. The upper panel of Fig. 6 shows how the various pressure components for H II regions within the LMC and SMC (green and red points, respectively) compare to those within the Milky Way Galactic Centre (blue points). The first thing to note about the comparison shown in Fig. 6 is that the H II regions within the LMC and SMC have systematically larger effective radii and lower pressures than the Galactic Centre H II regions. We find that the Galactic Centre H II regions extend to an effective radius of several parsecs (average of 4.5 pc from Table 1, while the sources within the SMC/LMC have average radii of around $\sim$50 pc, with several sources within the LMC extending out to radii well above 100 pc; comparable to the size of the entire Galactic Centre (see Fig. 1). It is interesting to compare these maximum sizes to the scales when the ambient pressure equals the observed internal pressures. Walker et al. (2018) estimate molecular clouds within the Galactic Centre are subjected to an external pressure of the order $P/k_{\rm B} \sim 10^{7-8}$ K cm^{-3}, whilst the external pressures found within LMC/SMC and Milky Way disc environments is typically at least two-to-three orders of magnitude lower ($P/k_{\rm B} \sim 10^{5}$ K cm^{-3}; Bertoldi & McKee 1992; Lada et al. 2008; Belloche et al. 2011; Field, Blackman & Keto 2011; Hughes et al. 2013). These ambient pressures are overlaid in Fig. 6 as horizontal grey dotted lines. We find that the ambient pressure for the Galactic Centre crosses the $P \propto r^{-1}$ relation at a radius of several parsecs, whilst the LMC/SMC ambient pressure crosses this relation at a radius of few hundred parsecs. These values are then broadly comparable to the observed maximum sizes of the H II regions within the two environments. This would suggest that the maximum size of the H II regions is set by the point where the internal and ambient pressure are equal, and hence the higher ambient pressure within the Galactic Centre is limiting the H II regions to a smaller size. The trend we observe cannot be due to the low angular resolution of the LMC/SMC observations. For example, 30 Doradus is a well studied H II region complex within the LMC, and has a resolved radius of $\sim$200 pc (Lopez et al. 2011), an order of magnitude larger than any resolved H ii regions within the Galactic Centre. However, we note that while this lack of large H II regions in the Galactic Centre is likely physical, the absence of small ones from the LMC/SMC samples is probably affected by resolution limits. The ATCA map used in Lopez et al. (2014) has a resolution of 22 arcsec $\sim$5 pc at the distance of the LMC, hence the Galactic Centre H II regions would be confined to a single pixel in their LMC map. The lower panel of Fig. 6 shows how the various pressure components compare irrespective of the host environment. We find that the pressure components broadly follow the previously discussed radial dependence (Section 2.2). We see that the direct radiation pressure follows a steep slope, from being the dominant pressure term at scales of $<$0.01 pc to becoming almost negligible at $\gg$1 pc scales. The remaining pressure terms appear to be approximately equal within an order of magnitude scatter, and show no appreciative decline as a function of the radius at $>$10 pc scales.

4.2 Comparison to expansion rates from analytic models

Many analytic models in the literature estimate the expansion rate of H II regions (e.g. Bisbas et al. 2015; Geen et al. 2019). In this section, we investigate how well the sizes of the Galactic Centre H II regions are predicted by several of the commonly used expansion

[6]We note that the direct radiation pressure calculated by McLeod et al. (2019) has been increased by a factor of three to match the definition outlined by Lopez et al. (2011, 2014), and this work (see equation 4).

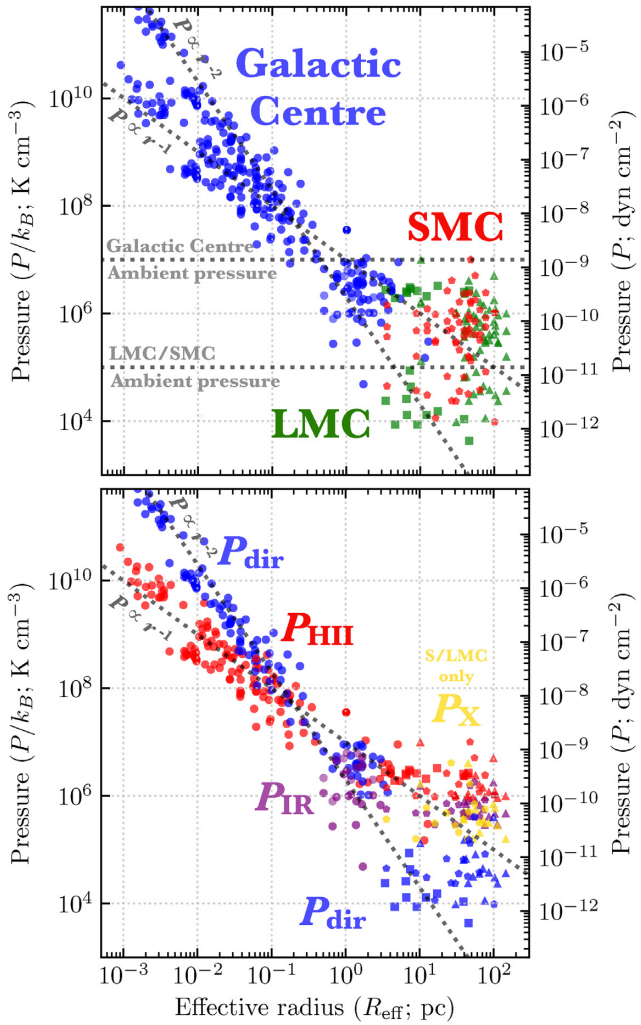

Figure 6. A comparison between the Galactic Centre, LMC and SMC (Lopez et al. 2011, 2014; McLeod et al. 2019). In the upper panel the points are differentiated in colour by their host environment, and in the lower panel the points are differentiated by the pressure component (as labelled). Circles show the pressure components determined in this work, pentagons are SMC sources from Lopez et al. (2014), triangles are LMC sources from Lopez et al. (2011, 2014), and squares are LMC sources from McLeod et al. (2019). We note that the hot X-ray emitting gas pressure component ($P_{\rm X}$) was not calculated within the CMZ due to the high extinction (Section 2.1), but we do show $P_{\rm X}$ determined for the LMC and SMC for comparison (Lopez et al. 2011, 2014). We show the ambient pressures determined for the Galactic Centre (Walker et al. 2018) and LMC (Hughes et al. 2013) as horizontal grey dotted lines. The diagonal grey dotted lines show the $P \propto r^{-1}$ and $P \propto r^{-2}$ relations.

models given assumptions about the age of each H II region. In doing so, we aim to test the importance of including the various pressure components into these analytic models. For brevity, we only introduce the final analytic solutions of each model below, and refer the interested reader to the original papers for full details. The simplest and mostly widely known of the expansion models that takes into account only the thermal pressure of the warm ionized gas was outlined by Spitzer (1978), and later modified by Dyson & Williams (1980). This model assumes an initially spherically symmetric cloud with a radius of $R_{\rm cl}$, a total mass of $M_{\rm cl}$ and a uniform density of $\rho_{\rm cl}$ containing atomic hydrogen with a uniform temperature of $T_{\rm cl}$. As shown by Strömgren (1939), the flux of high energy Lyman continuum photons, $\mathcal{N}_{\rm LyC}$, emitted by the central source will ionize a spherical region of radius,

$$R_{\rm st} = \left(\frac{3\mathcal{N}_{\rm LyC} m_{\rm p}^2}{4\pi\alpha_{\rm B}\rho_{\rm cl}^2}\right)^{1/3} = 0.57\left(\frac{\mathcal{N}_{\rm LyC}}{10^{50}{\rm s}^{-1}}\right)^{1/3}\left(\frac{\rho_{\rm cl}}{100{\rm M}_\odot{\rm pc}^{-3}}\right)^{-2/3}, \quad (12)$$

where $m_{\rm p}$ is the mass of a proton, and the recombination coefficient can be taken as $\alpha_{\rm B} \approx 2.7 \times 10^{-13}\,{\rm cm}^3\,{\rm s}^{-1}$. This simplified solution for $R_{\rm st}$ assumes an ISM that is composed solely of H, with no He. The so-called Spitzer solution to the variation in H II region radius with time is given as,

$$R_{\rm Sp}(t) = R_{\rm st}\left(1 + \frac{7}{4}\frac{\sigma_{\rm T,i}t}{R_{\rm st}}\right)^{4/7}, \quad (13)$$

where $\sigma_{\rm T,\,i}$ is the sound speed within the ionized gas ($\sim 8\,{\rm km\,s}^{-1}$ at 5000 K; see Section 2.1.1), and t the age of the H II region. For all analytic solutions presented in this section, we make the assumption that $T_{\rm cl}/T_{\rm H\,II} \ll 1$, where the $T_{\rm cl}$ is the neutral medium temperature and $T_{\rm H\,II}$ is the ionized gas temperature. Nonetheless, we consider that this may not hold within the Galactic Centre, where both the electron temperature is lower and the neutral gas temperature is higher; $T_{\rm cl}/T_{\rm H\,II} \sim 50\,{\rm K}/5000\,{\rm K} \sim 0.01$ (e.g. Mehringer et al. 1992; De Pree et al. 1996; Clark et al. 2013; Krieger et al. 2017). To test this, we use the integral of the full Spitzer solution given in Raga, Cantó & Rodríguez (2012, equations 9 and 10), and find an overall decrease in the predicted size of the H II regions of 1 and 10 per cent at times of 0.2 and 1.3 Myr, respectively. This deviation is well within the expected uncertainty on these analytic solutions inherited from the broad range of input parameters, and, therefore, continue to work under the assumption that the $T_{\rm cl}/T_{\rm H\,II} \ll 1$ simplification holds within the Galactic Centre. A second simple method for describing the expansion of an H II region is provided by Hosokawa & Inutsuka (2006), who used the equation of motion of the expanding shell to derive the time-dependent position of the ionization front. This solution can be given as,

$$R_{\rm H\&I}(t) = R_{\rm st}\left(1 + \frac{7}{4}\sqrt{\frac{4}{3}}\frac{\sigma_{\rm T,i}t}{R_{\rm st}}\right)^{4/7}. \quad (14)$$

This differs from equation (13) by a factor of $\sqrt{4/3}$, due to the inclusion of the inertia of the shocked gas (see Bisbas et al. 2015). This model also only accounts for the thermal pressure of the ionized gas. We note that the 'early phase' Spitzer (1978) and Hosokawa & Inutsuka (2006) solutions for thermal expansion have been chosen for their simplicity. However, we have shown that the H II regions studied here could be close to pressure equilibrium with their surrounding environment and, therefore, in a later stage of expansion. We note that there are analytic models that account for the swept-up material in the shell during the later expansion phase(s), which in effect slow the expansion rate for times larger than ~ 0.5 Myr (e.g. Raga et al. 2012; Williams et al. 2018). However, we will shortly show that the observed H II region sizes are typically unpredicted by the thermal expansion models. These late time solutions are, therefore, not considered within this section as the further slowing of the expansion rate would not provide a better agreement with the observations. A third model for the expansion of an H II region is proposed by Weaver et al. (1977). This solution accounts for the stellar wind pressure, and takes the following form (Tielens 2005),

$$R_{\rm W}(t) \simeq \left(\frac{2}{\pi}\frac{L_{\rm wind}}{\rho_0}t^3\right)^{1/5}, \simeq 32\left(\frac{L_{\rm wind}}{10^{36}\,{\rm erg\,s}^{-1}}\right)^{1/5}\left(\frac{n_{\rm cl}}{0.5\,{\rm cm}^{-3}}\right)^{-1/5}\left(\frac{t}{10^6{\rm yr}}\right)^{3/5}, \quad (15)$$

where $n_{\rm cl}$ is the initial molecular hydrogen number density of the host molecular cloud; i.e. $n_{\rm cl} = \rho_{\rm cl}/\mu_{\rm H_2} m_{\rm H}$, where $\mu_{\rm H_2} = 2.8$ is the mean molecular weight per hydrogen molecule, and $m_{\rm H} = 1.67 \times 10^{-24}$ g is the mass of atomic hydrogen. The wind mechanical luminosity, $L_{\rm wind}$, is obtained by considering the stellar population within each region. For each high mass star, $L_{\rm wind}$ can be expressed as,

$$L_{\rm wind} = \frac{1}{2}\dot{M} v_{\infty}^2 \, , \tag{16}$$

where $\dot{M}$ is the stellar wind mass-loss rate and v_{∞} is the terminal wind velocity. Following McLeod et al. (2019), we use the mass-loss rates and terminal velocities determined for a range of O-type stellar types from Muijres et al. (2012, Table 1).[7] We use the spectral classifications determined from the radio observations outlined in Table 2 to calculate the wind luminosity for the Galactic Centre sources (i.e. Mehringer et al. 1992; Schmiedeke et al. 2016). The final, more complex analytical models we consider were presented by Krumholz & Matzner (2009, Section 2, equations 11–13) and Kim, Kim & Ostriker (2016, Section 2, equations 1– 5, 10, and 13–16). These authors build upon the aforementioned solutions and account for both the thermal and radiation pressure contributions to the expansion. Moreover, Krumholz & Matzner (2009, Section 3) include trapping effects, where the feedback from the young stars is contained within the H II region bubble. The overpressure caused by the trapped energy results in a significantly increased expansion speed of the H II region. Fig. 7 shows the size as a function of age for each of the analytic models estimated using the range of observed properties within the Galactic Centre H II regions and their progenitor clouds. We adopt Lyman continuum ionization rates of $\mathcal{N}_{\rm LyC} = 0.08 \times 10^{50} {\rm s}^{-1}$ and $5 \times 10^{50} {\rm s}^{-1}$, which bracket the range of total ionization rates measured within G0.6 and Sgr B2, respectively. For Krumholz & Matzner (2009), we use bolometric luminosities of $L_{\rm bol} \sim 10^{6-7}\,{\rm L}_{\odot}$, which have been measured towards Sgr B2 and G0.6, respectively (see Barnes et al. 2017). For the Weaver et al. (1977) solution, we use wind luminosities of $L_{\rm wind} = 10\,{\rm L}_{\odot}$, $100\,{\rm L}_{\odot}$, and $4000\,{\rm L}_{\odot}$, which cover the measured range within G0.6, Sgr B1, and Sgr B2, respectively. For all the models we adopt the same initial cloud density of $\rho_{\rm cl} = 650\,{\rm M}_{\odot}\,{\rm pc}^{-3}$, or $n_{\rm cl} = 9.5 \times 10^3\,{\rm cm}^{-3}$, which corresponds to the lowest density estimated for the Galactic Centre precursor molecular clouds (i.e. $m_{\rm cl} \sim 1.5 \times 10^4\,{\rm M}_{\odot}$ and $r_{\rm cl} \sim 1.75$ pc for Cloud 'b'; Barnes et al. 2017). We use $r_{\rm cl}$ and $\rho_{\rm cl}$ as r_0 and ρ_0 for the Krumholz & Matzner (2009) solution, respectively. These values of $r_{\rm cl}$, $\rho_{\rm cl}$, $n_{\rm cl}$, $\mathcal{N}_{\rm LyC}$, $L_{\rm bol}$, and $L_{\rm wind}$ were chosen to give the most representative expansion rates for the Galactic Centre H II regions. Finally, for the Krumholz & Matzner (2009) solution,[8] we consider two physical scenarios, represented by two different values of the trapping parameter $f_{\rm trap}$. This parameter represents the factor by which the radiation–pressure force is enhanced by the trapping of energy within the expanding shell. Our first scenario is $f_{\rm trap} = 1$, which corresponds to every emitted photon being absorbed once in the shell and depositing its momentum there before escaping. Our second scenario is $f_{\rm trap} = 3$, which corresponds to a moderate amplification of the radiation force due to additional scattering of the IR photons produced by the initial absorption and re-emission, or due to the added pressure of hot stellar winds; in terms of pressures, $f_{\rm trap} = 3$ corresponds to $P_{\rm IR} = 2P_{\rm dir}$ or $P_X = 2P_{\rm dir}$. Krumholz & Matzner (2009) suggest that $f_{\rm trap}$ values of a few could be typical for a relatively non-porous shell, and this result is consistent within the uncertainties with our measured value of $P_{\rm IR}$. The corresponding range of predicted effective radii within the observational limits are plotted as a function of time as coloured shaded regions in Fig. 7. Note that the wind solution for Sgr B2 using $L_{\rm wind} = 4000\,{\rm L}_{\odot}$ has been plotted separately as a dashed red line. We compare the models to the observed sizes and ages of the Galactic Centre H II regions (see Table 4). We assume a ±20 per cent uncertainty on the age of the observed H II regions, and calculate the effective radius uncertainty from the semimajor and minor axis of an ellipse placed over the contour used to define each source (as outlined in Barnes et al. 2017; also shown on Fig. 1). Fig. 7 shows that all the expansion solutions do a reasonable job of predicting the sizes of the observed H II regions given that there has been no fine-tuning of the model parameters. The thermal and radiation pressure solutions reproduce the effective radius of G0.6 well. However, they underpredict the radius of Sgr B2, Sgr B1, and G0.3 by a factor of ∼3. We see that the wind and trapped radiation solutions match the radius of Sgr B2 (Weaver et al. 1977; Krumholz & Matzner 2009). Yet, only the Krumholz & Matzner (2009) trapped solution also matches the larger radii of Sgr B1 and G0.3. Bringing these results together suggests that a modest amount of trapping, either in the form of confined stellar winds or confined IR photons, is important at early times in driving

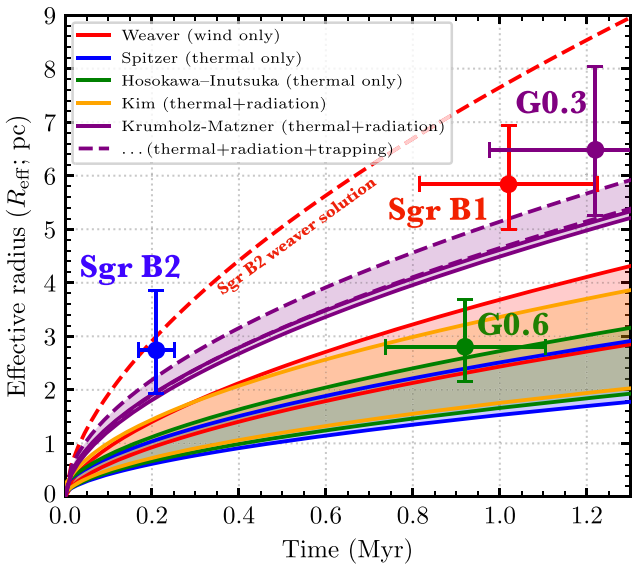

Figure 7. A comparison between the sizes of the observed Galactic Centre H II regions, and the predictions from theoretical models as a function of time (Section 4.2). The model predictions have been taken from Weaver et al. (1977), Spitzer (1978), Hosokawa & Inutsuka (2006), Krumholz & Matzner (2009), and Kim et al. (2016). These are shown as coloured shaded regions and lines (see legend). The shaded region represents the range of predicted effective radius at a given time within the observational limits for the observed initial cloud properties ($\rho_{\rm cl}$, $r_{\rm cl}$, $n_{\rm cl}$) and H II region properties ($\mathcal{N}_{\rm LyC}$, $L_{\rm bol}$, $L_{\rm wind}$, $f_{\rm trap}$). The dashed line shows the Weaver et al. (1977) wind solution using $L_{\rm wind}$ determined for the most massive H II region; Sgr B2 (see the text). We assume a ±20 per cent uncertainty on the age of the observed H II regions, and calculate the radius uncertainty from the semimajor and minor axis of an ellipse placed over the contour used to define each source (as outlined in Barnes et al. 2017).

[7] We assume that all the Galactic Centres H II regions contain supergiant stars, and use the last column in Muijres et al. (2012, Table 1) for $\dot{M}$, and compute the terminal velocity as 2.6 times the escape velocity (seventh column).

[8] In the models of Krumholz & Matzner (2009), we assume a constant initial density profile ($k_{\rho} = 0$), and the case of a blister H II region, or a constant of 1.9×10^{-2} in their equations (4) and (5). This constant has been reduced by a factor of 2.2^2 to account for the number of free particles per H nucleus (Fall, Krumholz & Matzner 2010).

the expansion of the H II regions. Wind feedback, however, needs to become weaker at later times (>0.2 Myr), to explain the large, more evolved H II regions. The Weaver et al. (1977) solution assumes that the wind gas is adiabatic and trapped, so it applies to a bubble that is completely closed and has no cooling. As soon as gas breaks out, or there is significant mixing between hot and cold gas that leads to cooling, the expansion speed will drop below the Weaver et al. (1977) solution. There is evidence of such strong energy loss from winds for porous H II regions outside of the Galactic Centre (Harper-Clark & Murray 2009; Rosen et al. 2014). This porosity could be caused by stellar feedback punching holes in the H II shell or expansion into a non-uniform (turbulent) medium, and can occur relatively early within the H II region's lifetime (<1 Myr). It is entirely possible, however, that in the high-density environment of the Galactic Centre, the winds stay contained within the shell longer, which could lead to a more prolonged expansion. In summary, we propose that Fig. 7 shows evidence for an energy-driven phase of expansion, where either photons or hot gas are contained within the H II regions, but this phase must end by the time the H II region is $\sim$1 Myr old. This time-scale is shorter than the predicted cloud lifetime in the Galactic Centre environment (Jeffreson et al. 2018), again implying that stellar feedback is also an important driver of the cloud lifecycle under high-pressure conditions. Finally, in this section, we assess if the large scale expansion of these H II regions has indeed stalled, as is suggested by the balance of their internal pressure components with the surrounding Galactic Centre environment (Section 4.1). To do so, we follow Bisbas et al. (2015) and calculate the stalling radius, $R_{\rm stall}$, as $R_{\rm stall,\,Sp} = R_{\rm st}(\sigma_{\rm T,\,i}/\sigma_{\rm T,\,n})^{4/3}$ for the Spitzer (1978) solution, and $R_{\rm stall,H\&I} = R_{\rm st}(\sigma_{\rm T,i}/\sigma_{\rm T,n})^{4/3}(8/3)^{2/3}$ for the Hosokawa & Inutsuka (2006) solution. In these equations, $\sigma_{\rm T,i} \sim 8\,{\rm km\,s^{-1}}$ and $\sigma_{\rm T,n} \sim \sqrt{T_{\rm cl}k_{\rm B}/m_{\rm H}\mu_{\rm H_2}} \sim 0.4\,{\rm km\,s^{-1}}$ are the sound speed in the ionized and neutral gas, respectively (where $\mu_{\rm H_2} = 2.37$). Using the same parameter ranges assumed above, we calculate $R_{\rm stall,\,Sp} =$ 4–12 pc and $R_{\rm stall,H\&I} = 8 - 23$ pc. These cover the measured size range of $\sim 2 - 7$ pc for the Galactic Centre H II regions (see Fig. 7). Therefore, this analysis further supports that the Galactic Centre H II regions, particularly the largest of these (Sgr B1 and G0.3), may have reached pressure equilibrium with their surrounding environment, and could, therefore, have now stopped expanding.

4.3 Comparison to feedback simulations

In this section, we compare the observed Galactic Centre H II regions to a set of feedback simulations to better understand the evolution of internal pressure components. To do so, we make use of the smoothed particle hydrodynamics simulations described in Dale et al. (2012), specifically their Run F simulation. Run F models a sub-virial turbulent 10^5 $M_\odot$ cloud with an initial radius of 10 pc. Such a massive and dense cloud in principle offers a realistic comparison with typical Galactic Centre clouds. The simulations presented in Dale et al. (2012) allow star formation to initiate, and then model the effects of photoionization feedback to examine the dynamical effects of the expansion of the H II regions. Star formation occurs at many different locations within the cloud, resulting in several distinct sources of ionizing radiation. We choose to focus on the snapshot of the Run F simulations at 0.78 Myr after the formation of the first O–stars and the initiation of ionization feedback, as this approximately corresponds to the average age of the Galactic Centre H II regions ($\sim$0.8 Myr). We extracted the ionized gas from the snapshot and computed a map of the emission measure integrating along the z-axis by integrating the electron density. To produce mock observations, we then convert the emission measure values into units of flux density following the conversions of Mezger & Henderson (1967, e.g. also see equation 6 of Schmiedeke et al. 2016). We assume a temperature of 10^4 K, a source distance of 8.5 kpc, a beam size of 5 arcsec, and a frequency of 5 GHz. The latter two of these parameters were chosen such that we can make a direct visual comparison to some example 5 GHz VLA observations of the Sgr B1 source (Butterfield et al., in preparation), which is the closest in estimated age to the simulation snapshot. Fig. 8 shows the Sgr B1 VLA observations and the simulated observations over the same angular scale, set to the same colour scale and overlaid with equivalent contour levels. Here, we see similarly compact structures within the two maps that have peak fluxes $\sim$0.1 Jy beam^{-1} and sizes of $\sim$ 1pc.[9] On the large scale, there appears to be significantly more extended emission within the VLA observations. We believe that this may be due the simulated cloud having no external pressure confining it, so that diffuse ionized gas can leak away to large radii and achieve very low densities. It may also be related to the complex environment of the Galactic Centre, which makes it difficult to determine what fraction of the diffuse component is physically associated with the compact sources. To make a direct comparison to the internal pressures within the observed H II regions, we apply the same analysis presented in Section 2.1 to the simulated 5 GHz observations. Specifically, we smooth the simulation map to the same resolution as the data, and then run a dengrodram analysis on it using the same parameters we use on observations.[10] We then extract the scale-dependent pressures using the same two methods described in sections 2.1.1 and 2.1.2. The right-hand panel of Fig. 8 shows the components of the internal pressure calculated for the Galactic Centre observations and the simulated observations as a function of radius. Again, we find a nice agreement between the simulations and observations. The match is particularly good on the smallest spatial scales ($\sim$0.1 pc), where we have good crossover in spatial scale between the two data sets. Moreover, it is interesting that the simulations recover the anticorrelation of decreasing pressure with increase size-scale seen in the observations, and appear to have the slope between $P \propto r^{-1}$ and $P \propto r^{-2}$ (compare to the overplotted dashed lines). In the simulations, the ionizing sources at this epoch are still embedded in, or at least close to, the dense, cold filaments in which star formation in the cloud is initiated. It is this gas which is being ionized, and recently ionized gas, therefore, has high densities. However, the ionized gas rapidly expands into lower-density regions of the cloud, and eventually leaves the cloud entirely, forming an ionized flow (i.e. driven by the thermal ionized gas pressure $P_{\rm H\,II}$) with an expansion velocity on the order of 10 km s^{-1}. We suggest that this may be an explanation of the relation between pressure and size-scale seen in the Galactic Centre clouds. They may also be the result of recently formed massive stars which are still disrupting the small, dense gaseous structures in which most of the star formation in their host clouds is occurring, by driving pc scale ionized outflows which disperse the ionized gas to large scales and lower densities and pressures.

4.4 Energy and momentum budget

Within this section, we assess the coupling efficiency between the total energy injected by the stellar population within the Galactic

[9]The spatial resolution of both maps is $\sim$0.2 pc, which limits the identification of any ultracompact H II regions seen in Sgr B2 by e.g. De Pree, Goss & Gaume (1998).

[10]The following set of parameters are used for determination of the dendrogram structure from the simulations: min_value $= 10\,\sigma$ ~ 0.04 mJy beam^{-1}; min_delta $= 10\,\sigma$; min_delta $= 1$ beam ~ 25 pixels.

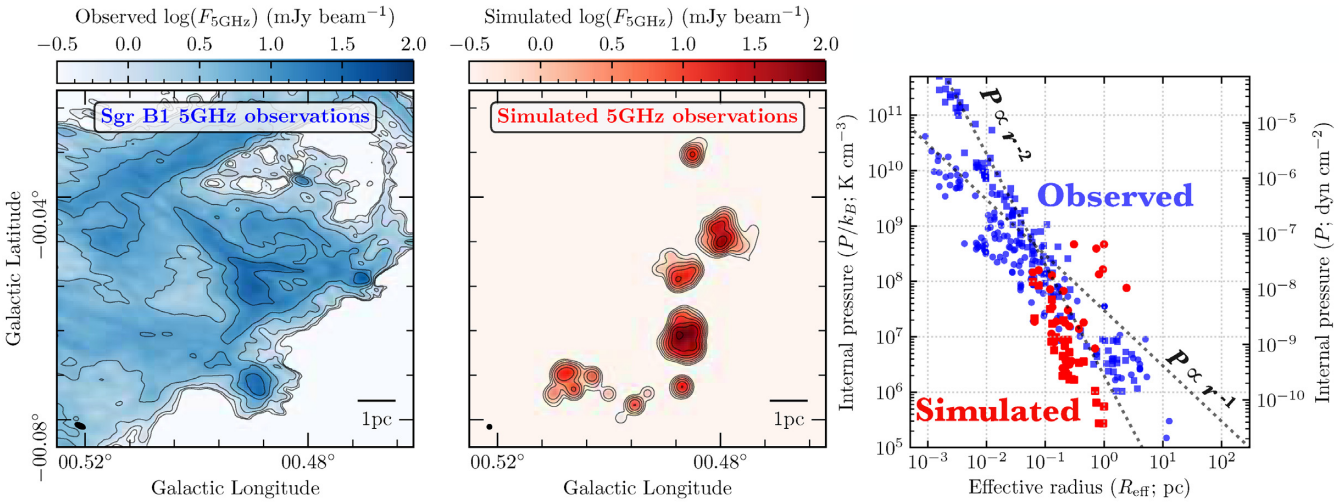

Figure 8. A comparison between a Galactic Centre H II region and mock observations taken from the feedback simulations (see Section 4.3). The left-hand panel shows a 5 GHz continuum map taken with the VLA towards the Sgr B1 region (Butterfield et al., in preparation), while the central panel is a snapshot from the simulations at a time of ∼0.8 Myr, approximately corresponding to the assumed age of Sgr B1 (see Table 1). The simulations have been converted from emission measure units to units of flux densities following Mezger & Henderson (1967). To allow a direct comparison to the observations, the colour scale limits are the same for both maps. Contours show isosurfaces of log (F_{5GHz}) at intervals of 0.35 dex; the lowest contour corresponds to $10^{-0.5}$ mJy beam^{-1}, and the highest to 10^{2} mJy beam^{-1}. The right-hand panel shows a comparison between the observed and simulated internal pressure components as a function of the H II region effective radius. Here, only the warm ionized thermal pressure ($P_{H\,II}$; circles) and the direct radiation pressure (P_{dir}; squares) are shown. Note that for the simulated pressures, the largest values were obtained by running our source identification and analysis on spatially smoothed versions of the simulated map shown in the central panel. In doing so, these simulated values offer a direct comparison to the method used to analyse the observed H II regions at increasing (or lower) resolutions within each source. The overlaid diagonal lines shows $P \propto r^{-1}$ and $P \propto r^{-2}$ for reference (note that these are not fits to the data).

Centre H II regions, and the observed energy and momentum of the H II regions (Section 3.2). To determine the total energy injection by the stellar population within each H II region, we simply assume that the luminosity emitted over the lifetime of the stellar population within the H II region could be theoretically used to directly drive its expansion. The coupling efficiency in this case would be $\epsilon_E = E_{obs}/E_{tot}$, where E_{obs} is the observed kinetic energy of the expanding shell (Section 3.2), and E_{tot} is the total energy,

$$E_{tot} = L_{bol} t_{age}, \tag{17}$$

where t_{age} is the age given in Table 1. To determine the total L_{bol} for Sgr B2, G0.6, and Sgr B1 we use the highest resolution and quality H II region catalogues available for each source within the literature (Mehringer et al. 1992; Schmiedeke et al. 2016). We use the stellar parameters of O and early B type stars determined by Vacca, Garmany & Shull (1996, table 5) to convert the catalogued ZAMS type to a bolometric luminosity. We then sum these individual luminosities to get total bolometric luminosities of $10^{6.5}$ L$_\odot$, $10^{5.3}$ L$_\odot$, and $10^{5.7}$ L$_\odot$ for Sgr B2, G0.6, and Sgr B1, respectively. Given that approximately $L \propto M^{3.5}$, we do not account for the contribution to the total luminosity from lower mass stars not observed in the radio continuum (i.e. those with $M < 8$ M$_\odot$). Using the bolometric luminosities in the above equations gives total energies of $10^{45.9}$, $10^{45.3}$, and $10^{45.8}$ J for Sgr B2, G0.6, and Sgr B1, respectively. Comparing these to the observed energies given in Table 4, we calculate energy coupling efficiencies of $\epsilon_E = E_{obs}/E_{tot}$ of 7×10^{-5}, 15×10^{-5}, 24×10^{-5} for Sgr B2, G0.6, and Sgr B1, respectively. These results are summarized in Table 5. In short, we find that only a very small fraction of the total energy released by the young stellar populations studied here goes into driving the expansion of the H II regions. We expect then that the vast majority of the energy coming out either goes into ionization or is just starlight that we observe.

Table 5. Total bolometric luminosity, energy output, energy coupling,[a] and the momentum efficiency factor[b] for each of the Galactic Centre H II region (Section 4.4).

Source	log(L_{bol}) (L$_\odot$)	log(E_{tot}) (J)	ϵ_E [a] (10^{-5})	ψ_W [b]
Sgr B2	6.51	45.92	6.9	3.5
G0.6	5.26	45.31	14.7	29.5
Sgr B1	5.72	45.81	24.4	19.8

Notes.[a] $\epsilon_E = E_{exp}/E_{tot}$ or fraction of energy output by embedded stellar population that have driven the expansion of the H II region (see Table 4).
[b] $\psi_W = p_{exp}/(L_{bol} c t_{age})$ or the momentum in expanding shell to the momentum carried by the radiation field.

We also assess the momentum budget of the embedded stellar populations with respect to their expanding H II regions. To do so, we follow Dekel & Krumholz (2013), and calculate the momentum efficiency factor, or the ratio of momentum in the expanding shell to the momentum carried by the radiation field. We define this as the dimensionless factor $\psi_W = p_{exp}/(L_{bol} c t_{age})$, which describes the relative importance of either the radiation field ($\psi_W < 1$) or the thermal pressure ($\psi_W > 1$) in driving the expansion of the H II region. The parameters for this calculation are given in Tables 4 and 5. We find that $\psi_W \sim 4$, 30, and 20 for Sgr B2, G0.6, and Sgr B1, respectively (see Table 5). Therefore, ψ_W is larger than unity for all the Galactic Centre H II regions, highlighting that winds cannot provide the energy required for the observed expansion and the regions should be thermal pressure dominated. This result is in-line with the H II regions having a larger warm ionized gas pressure components compared to direct radiation pressures when measured over similar scales of ∼ 1 pc (see Fig. 3). Additionally, it is interesting that we find the that the youngest H II region (Sgr B2; 0.2 Myr) has a

significantly smaller momentum efficiency factor than the older H II regions (e.g. Sgr B1; ~ 1 Myr). This could be evidence to show that H II regions become more thermal pressure dominated, as opposed to radiation pressure dominated, as they expand and evolve.

5 CONCLUSIONS

SNe are thought to play a major role in the self-regulation of star formation in galaxies across cosmic time (McKee & Ostriker 1977; Mac Low & Klessen 2004; Klessen & Glover 2016). However, the efficiency with which SNe energy and momentum couples to the local galactic environment strongly depends on the density distribution of the surrounding ISM (see Girichidis et al. 2016 and references therein). Feedback processes from the pre-SNe stages of high-mass stars play a significant role in determining the environment into which SNe subsequently explode. Studying these earliest stages of stellar feedback is then crucial to understanding the coupling of SNe to their environment, and hence their contribution to the energy cycle of star formation in galaxies. There are observational constraints on the magnitudes and time-scales of early stellar feedback in low ISM pressure environments (e.g. Kruijssen et al. 2019b; Chevance et al. 2020c, b), yet no such constraints exist for more cosmologically typical high ISM pressure environments. In this work, we aim to address this by studying the early evolutionary stages (pre-SNe) of stellar feedback within the central $\sim$100 pc of the Milky Way's Galactic Centre. We investigate the dominant pressures within H II regions using the methods outlined by Lopez et al. (2011, 2014), and McLeod et al. (2019). These authors calculate the four sources of pressure responsible for the expansion of H II regions as: thermal pressure from the warm (10^4 K) ionized gas ($P_{\rm H\,II}$), direct radiation pressure from the luminous stellar population ($P_{\rm dir}$), pressure from the photons released by heated dust ($P_{\rm IR}$), and thermal pressure from the shock heated (10^6 K) X-ray emitting gas ($P_{\rm X}$). Here we calculate three of these, $P_{\rm H\,II}$, $P_{\rm dir}$, and $P_{\rm IR}$ within four large, Galactic Centre H II region complexes (see Fig. 3); $P_{\rm X}$ is unfortunately inaccessible due to the very large extinction and strong foreground towards the Galactic Centre at soft X-ray wavelengths. We plot the pressure terms as a function of size scale, and find mean radial dependence of $P_{\rm HII} \propto R_{\rm eff}^{-1}$, and $P_{\rm dir} \propto R_{\rm eff}^{-1.5}$ (see Fig. 4). As a result of this radial variation, $P_{\rm dir}$ dominates on the small scales (0.01 pc), $P_{\rm dir} \sim P_{\rm HII}$ on the intermediate scales (0.01–0.1 pc), and on the large ($>$1 pc) scales $P_{\rm H\,II} > P_{\rm IR} \sim P_{\rm X} > P_{\rm dir}$ (Section 2.1). Comparing to H II regions within the Large and Small Magellanic Clouds (LMC and SMC, respectively), where the ambient pressure is 2–3 orders of magnitude smaller than the $\sim 10^{7-8}$ K cm^{-3} found in the Galactic Centre, we find that the radius at which H II regions reach pressure balance with their environments is $\sim$2–3 pc in the Galactic Centre, versus $>$100 pc in the Magellanic Clouds (Section 4.1). Given that the maximum sizes of H II regions in the Galactic Centre and LMC/SMC match the radius at which the internal pressure matches the ambient ISM pressure, we suggest that this shows the H II regions sizes are set by the point of pressure equilibrium with the ambient medium (see Fig. 6). We also compare our results to the predictions of models for H II region expansion driven by thermal pressure of the ionized gas, radiation pressure including trapping effects, or stellar winds (see Fig. 7). Combining observed sizes with H II region ages estimated from orbital modelling (Longmore et al. 2013b; Kruijssen et al. 2015), we find that three of the four H II regions have radii that are best fit by solutions with a moderate amount of boosting by trapped wind or radiation energy. Wind models where the hot gas is purely adiabatic (e.g. Weaver et al. 1977) tend to overpredict H II region radii, while those assuming expansion driven solely by direct starlight or warm gas pressure (e.g. Hosokawa & Inutsuka 2006; Kim et al. 2016) underpredict them. The best-fitting results come from the Krumholz & Matzner (2009) model with moderate trapping of wind or IR radiation energy ($f_{\rm trap} \sim 3$ in their notation). Consistent with this conclusion, direct measurement of the momentum budget of the expanding shells suggests that they typically carry $\sim$10 times the momentum of the direct radiation field, again suggesting that modest amounts of trapped energy are boosting the expansion rate. We also compare to a set of smoothed particle hydrodynamics simulations including photoionization feedback (Dale et al. 2012). Analysis of synthetic radio maps from the simulation show excellent agreement with the small-scale morphology of the observed H II regions as a function of effective radius. In the simulations, the embedded stellar population is ionizing small-scale dense gaseous structures from which stars are forming, and then the ionized gas is dispersing to larger scales and lower densities and pressures. This produces a $P \propto r^{-2}$ profile comparable to that seen in the observations, suggesting that this profile may be an imprint of escaping photoionized gas. In all, we find that the Galactic Centre H II regions are dominated by the direct radiation pressure on only the smallest scales ($<$0.01 pc), and at all larger scales they appear to dominated by the thermal pressure of the ionized gas ($>$0.01–10 pc); there is evidence for a modest contribution from trapped IR radiation or hot stellar wind gas early in the expansion, but by significantly less than would be expected for efficient trapping. We see a link between the ages of the H II regions and the relative importance of both the direct and thermal expansion, which suggest that as the H II regions evolve they also become further dominated by the ionized gas thermal pressure. We find that the thermal pressure-driven expansion then reaches a point of pressure equilibrium with the surrounding environment, at which point further expansion is halted. The high ambient pressure within the Galactic Centre then naturally explains the systematically smaller H II regions compared to those observed with in the LMC and SMC. In view of the striking similarity between the H II region radii and the radius at which the region pressure drops to the ambient pressure, we hypothesize that star formation proceeds until the gas inflow can be halted, irrespective of the environment. In this case, star formation and feedback self-regulate such that each cloud attains the integrated star formation efficiency required for blowout, which happens when the nascent stellar population can drive the H II region radius to the cloud (or gas disc) scale height. A similar conclusion was recently reached for giant molecular clouds in NGC 300, which have a mean separation length that closely matches the gas disc scale height, suggesting that their in-plane spacing is set by feedback bubbles breaking out of the disc (Kruijssen et al. 2019b). Interestingly, the H II region expansion velocities measured across the nearby galaxy population are highly similar to the ones obtained here for the Galactic Centre and have also been attributed to thermal feedback (Kruijssen et al. 2019b; Chevance et al. 2020c, a; McLeod et al. 2020). Together with this work, these studies provide evidence for feedback-regulated cloud lifecycles, with surprisingly universal characteristics over three orders of magnitude in ambient gas pressure.

ACKNOWLEDGEMENTS

We would like to thank the referee for their constructive feedback that helped improve the paper. We would also like to thank Jonathan Henshaw and Jeong-Gyu Kim for their enlightening discussions on the paper, and Natalie Butterfield and collaborators for providing the 5 GHz VLA continuum observations shown in this work (project ID: 17A-321). ATB and FB would like to acknowledge funding

from the European Research Council (ERC) under the European Union's Horizon 2020 research and innovation programme (grant agreement No. 726384/Empire). MRK acknowledges support from the Australian Research Council through its Discovery Projects (award DP190101258) and Future Fellowship (award FT180100375) funding schemes, and from the Alexander von Humboldt Foundation through a Humboldt Research Award. JMDK gratefully acknowledges funding from the Deutsche Forschungsgemeinschaft (DFG, German Research Foundation) through an Emmy Noether Research Group (grant number KR4801/1-1) and the DFG Sachbeihilfe (grant number KR4801/2-1), as well as from the European Research Council (ERC) under the European Union's Horizon 2020 research and innovation programme via the ERC Starting Grant MUSTANG (grant agreement number 714907). In this work we use data that were obtained using the Mopra radio telescope, a part of the Australia Telescope National Facility which is funded by the Commonwealth of Australia for operation as a National Facility managed by CSIRO. The University of New South Wales (UNSW) digital filter bank (MOPS) used for the observations with Mopra was provided with support from the Australian Research Council (ARC), UNSW, Sydney, and Monash Universities, as well as the CSIRO.

DATA AVAILABILITY

A full machine-readable version of Table A1 is available in the online supplementary of this work. The data underlying this article will be shared on reasonable request to the corresponding author.

REFERENCES

Agertz O., Kravtsov A. V., Leitner S. N., Gnedin N. Y., 2013, ApJ, 770, 25
Anderson L. D. et al., 2020, ApJ, preprint (arXiv:2008.04258)
Barnes A. T. et al., 2019, MNRAS, 486, 283
Barnes A. T., Longmore S. N., Battersby C., Bally J., Kruijssen J. M. D., Henshaw J. D., Walker D. L., 2017, MNRAS, 469, 2263
Battersby C. et al., 2020, ApJS, 249, 35
Belloche A., Parise B., Schuller F., André P., Bontemps S., Menten K. M., 2011, A&A, 535, A2
Benson J. M., Johnston K. J., 1984, ApJ, 277, 181
Bertoldi F., McKee C. F., 1992, ApJ, 395, 140
Bisbas T. G. et al., 2015, MNRAS, 453, 1324
Blitz L., Rosolowsky E., 2006, ApJ, 650, 933
Cardelli J. A., Clayton G. C., Mathis J. S., 1989, ApJ, 345, 245
Carey S. J. et al., 2009, PASP, 121, 76
Caswell J. L., Haynes R. F., 1987, A&A, 171, 261
Chapman N. L., Mundy L. G., Lai S.-P., Evans N. J. II, 2009, ApJ, 690, 496
Chevance M. et al., 2016, A&A, 590, A36
Chevance M. et al., 2020a, MNRAS, submitted
Chevance M. et al., 2020b, Space Sci. Rev., 216, 50
Chevance M. et al., 2020c, MNRAS, 493, 2872
Churchwell E. et al., 2009, PASP, 121, 213
Clark P. C., Glover S. C. O., Ragan S. E., Shetty R., Klessen R. S., 2013, ApJ, 768, L34
Comerón S., Knapen J. H., Beckman J. E., Laurikainen E., Salo H., MartÃnez-Valpuesta I., Buta R. J., 2010, MNRAS, 402, 2462
Cram L. E., Claussen M. J., Beasley A. J., Gray A. D., Goss W. M., 1996, MNRAS, 280, 1110
Dale J. E., Ercolano B., Bonnell I. A., 2012, MNRAS, 424, 377
Dale J. E., Ercolano B., Bonnell I. A., 2013, MNRAS, 430, 234
Dale J. E., Kruijssen J. M. D., Longmore S. N., 2019, MNRAS, 486, 3307
De Pree C. G., Gaume R. A., Goss W. M., Claussen M. J., 1996, ApJ, 464, 788
De Pree C. G., Goss W. M., Gaume R. A., 1998, ApJ, 500, 847
Deharveng L., Peña M., Caplan J., Costero R., 2000, MNRAS, 311, 329
Dekel A., Krumholz M. R., 2013, MNRAS, 432, 455
Downes D., Maxwell A., 1966, ApJ, 146, 653
Downes D., Maxwell A., Rinehart R., 1970, ApJ, 161, L123
Draine B. T., 2003, ARA&A, 41, 241
Draine B. T., Li A., 2007, ApJ, 657, 810
Dutra C. M., Ortolani S., Bica E., Barbuy B., Zoccali M., Momany Y., 2003, A&A, 408, 127
Dyson J. E., Williams D. A., 1980, Physics of the Interstellar Medium. CRC Press, USA
Espinoza P., Selman F. J., Melnick J., 2009, A&A, 501, 563
Faesi C. M., Lada C. J., Forbrich J., 2018, ApJ, 857, 19
Fall S. M., Krumholz M. R., Matzner C. D., 2010, ApJ, 710, L142
Federrath C., Klessen R. S., 2012, ApJ, 761, 156
Field G. B., Blackman E. G., Keto E. R., 2011, MNRAS, 416, 710
Figer D. F., McLean I. S., Morris M., 1999, ApJ, 514, 202
Fitzpatrick E. L., 1999, PASP, 111, 63
Fujimoto Y., Chevance M., Haydon D. T., Krumholz M. R., Kruijssen J. M. D., 2019, MNRAS, 487, 1717
Gaume R. A., Claussen M. J., 1990, ApJ, 351, 538
Geen S., Pellegrini E., Bieri R., Klessen R., 2020, MNRAS, 492, 915
Genzel R. et al., 2011, ApJ, 733, 101
Girichidis P. et al., 2016, MNRAS, 456, 3432
Giveon U., Sternberg A., Lutz D., Feuchtgruber H., Pauldrach A. W. A., 2002, ApJ, 566, 880
Gravity Collaboration et al., 2018, A&A, 615, L15
Grudić M. Y., Hopkins P. F., Faucher-Giguère C.-A., Quataert E., Murray N., Kereš D., 2018, MNRAS, 475, 3511
Harfst S., Portegies Zwart S., Stolte A., 2010, MNRAS, 409, 628
Harper-Clark E., Murray N., 2009, ApJ, 693, 1696
Henshaw J. D. et al., 2016a, MNRAS, 457, 2675
Henshaw J. D. et al., 2019, MNRAS, 485, 2457
Henshaw J. D., Longmore S. N., Kruijssen J. M. D., 2016b, MNRAS, 463, L122
Hobbs R. W., Johnston K. J., 1971, ApJ, 163, 299
Hobbs R. W., Modali S. B., Maran S. P., 1971, ApJ, 165, L87
Hosokawa T., Inutsuka S.-i., 2006, ApJ, 646, 240
Hughes A. et al., 2013, ApJ, 779, 46
Jeffreson S. M. R., Kruijssen J. M. D., Krumholz M. R., Longmore S. N., 2018, MNRAS, 478, 3380
Jeffreson S. M. R., Kruijssen J. M. D., Keller B. W., Chevance M., Glover S. C. O., 2020, MNRAS, 498, 385
Jones P. A., Burton M. G., Cunningham M. R., Tothill N. F. H., Walsh A. J., 2013, MNRAS, 433, 221
Keller B. W., Kruijssen J. M. D., Wadsley J. W., 2020, MNRAS, 493, 2149
Keto E., Zhang Q., Kurtz S., 2008, ApJ, 672, 423
Kim J.-G., Kim W.-T., Ostriker E. C., 2016, ApJ, 819, 137
Kim J.-G., Kim W.-T., Ostriker E. C., 2018, ApJ, 859, 68
Klessen R. S., Glover S. C. O., 2016, Saas-Fee Advanced Course, 43, 85
Krieger N. et al., 2017, ApJ, 850, 77
Krieger N. et al., 2020, ApJ, 899, 158
Kruijssen J. M. D. et al., 2019a, MNRAS, 484, 5734
Kruijssen J. M. D. et al., 2019b, Nature, 569, 519
Kruijssen J. M. D., Longmore S. N., 2013, MNRAS, 435, 2598
Kruijssen J. M. D., Dale J. E., Longmore S. N., 2015, MNRAS, 447, 1059
Kruijssen J. M. D., Longmore S. N., Elmegreen B. G., Murray N., Bally J., Testi L., Kennicutt R. C., 2014, MNRAS, 440, 3370
Krumholz M. R. et al., 2014, in Beuther H., Klessen R. S., Dullemond C. P., Henning T., eds, Protostars and Planets VI. University of Arizona Press, Tucson, AZ, p. 243
Krumholz M. R., Kruijssen J. M. D., 2015, MNRAS, 453, 739
Krumholz M. R., Matzner C. D., 2009, ApJ, 703, 1352
Krumholz M. R., McKee C. F., 2005, ApJ, 630, 250
Lada C. J., Muench A. A., Rathborne J., Alves J. F., Lombardi M., 2008, ApJ, 672, 410
Lang C. C., Goss W. M., Wood O. S., 1997, ApJ, 474, 275
Lang C. C., Goss W. M., Morris M., 2001, AJ, 121, 2681
Law C., Yusef-Zadeh F., 2005, in Sjouwerman L. O., Dyer K. K., eds, X-Ray and Radio Connections. NRAO, New Mexico, USA, p. 3
Lee E. J., Murray N., Rahman M., 2012, ApJ, 752, 146
Li H., Vogelsberger M., Marinacci F., Gnedin O. Y., 2019, MNRAS, 487, 364
Lis D. C., Menten K. M., Serabyn E., Zylka R., 1994, ApJ, 423, L39

Little A. G., 1974, in Kerr F. J., Simonson S. C., eds, Proc. IAU Symp. 60, Galactic Radio Astronomy. D. Reidel Pub. Co, Dordrecht-Holland, Boston, p. 491
Longmore S. N. et al., 2012, ApJ, 746, 117
Longmore S. N. et al., 2013a, MNRAS, 429, 987
Longmore S. N. et al., 2013b, MNRAS, 433, L15
Lopez L. A., Krumholz M. R., Bolatto A. D., Prochaska J. X., Ramirez-Ruiz E., 2011, ApJ, 731, 91
Lopez L. A., Krumholz M. R., Bolatto A. D., Prochaska J. X., Ramirez-Ruiz E., Castro D., 2014, ApJ, 795, 121
Mac Low M.-M., Klessen R. S., 2004, Rev. Mod. Phys., 76, 125
McKee C. F., Ostriker J. P., 1977, ApJ, 218, 148
McLeod A. F. et al., 2020, ApJ, 891, 25
McLeod A. F., Dale J. E., Evans C. J., Ginsburg A., Kruijssen J. M. D., Pellegrini E. W., Ramsay S. K., Testi L., 2019, MNRAS, 486, 5263
Mehringer D. M., Yusef-Zadeh F., Palmer P., Goss W. M., 1992, ApJ, 401, 168
Mezger P. G., Henderson A. P., 1967, ApJ, 147, 471
Mezger P. G., Pankonin V., Schmid-Burgk J., Thum C., Wink J., 1979, A&A, 80, L3
Molinari S. et al., 2010, PASP, 122, 314
Molinari S. et al., 2011, ApJ, 735, L33
Morris M., Serabyn E., 1996, ARA&A, 34, 645
Muijres L. E., Vink J. S., de Koter A., Müller P. E., Langer N., 2012, A&A, 537, A37
Nobukawa M. et al., 2008, PASJ, 60, 191
Oey M. S., 1996a, ApJ, 465, 231
Oey M. S., 1996b, ApJ, 467, 666
Pellegrini E. W. et al., 2007, ApJ, 658, 1119
Pellegrini E. W., Baldwin J. A., Ferland G. J., 2010, ApJS, 191, 160
Pellegrini E. W., Baldwin J. A., Ferland G. J., 2011, ApJ, 738, 34
Ponti G. et al., 2015, MNRAS, 454, 1525
Purcell C. R. et al., 2012, MNRAS, 426, 1972
Raga A. C., Cantó J., Rodríguez L. F., 2012, MNRAS, 419, L39
Reid M. J. et al., 2014, ApJ, 783, 130
Reid M. J., Dame T. M., Menten K. M., Brunthaler A., 2016, ApJ, 823, 77
Roelfsema P. R., Goss W. M., Whiteoak J. B., Gardner F. F., Pankonin V., 1987, A&A, 175, 219
Rosen A. L., Lopez L. A., Krumholz M. R., Ramirez-Ruiz E., 2014, MNRAS, 442, 2701
Rosolowsky E. W., Pineda J. E., Kauffmann J., Goodman A. A., 2008, ApJ, 679, 1338
Rybicki G. B., Lightman A. P., 1979, Radiative Processes in Astrophysics. Wiley, New York
Schmiedeke A. et al., 2016, A&A, 588, A143
Schödel R., Najarro F., Muzic K., Eckart A., 2010, A&A, 511, A18
Shaver P. A., McGee R. X., Newton L. M., Danks A. C., Pottasch S. R., 1983, MNRAS, 204, 53
Sormani M. C., Barnes A. T., 2019, MNRAS, 484, 1213
Sormani M. C., Treß R. G., Ridley M., Glover S. C. O., Klessen R. S., Binney J., Magorrian J., Smith R., 2018, MNRAS, 475, 2383
Sormani M. C., Tress R. G., Glover S. C. O., Klessen R. S., Battersby C. D., Clark P. C., Hatchfield H. P., Smith R. J., 2020, MNRAS, 497, 5024
Spitzer L., 1978, Physical Processes in the Interstellar Medium. WILEY-VCH Verlag, Weinheim, Germany
Stinson G. S., Brook C., Macciò A. V., Wadsley J., Quinn T. R., Couchman H. M. P., 2013, MNRAS, 428, 129
Strömgren B., 1939, ApJ, 89, 526
Sun J. et al., 2018, ApJ, 860, 172
Sun J. et al., 2020, ApJ, 892, 148
Swinbank A. M. et al., 2011, ApJ, 742, 11
Swinbank A. M., Smail I., Sobral D., Theuns T., Best P. N., Geach J. E., 2012, ApJ, 760, 130
Tacconi L. J. et al., 2013, ApJ, 768, 74
Tielens A. G. G. M., 2005, The Physics and Chemistry of the Interstellar Medium. Cambridge University Press, Cambridge
Tress R. G., Sormani M. C., Glover S. C. O., Klessen R. S., Battersby C. D., Clark P. C., Hatchfield H. P., Smith R. J., 2020, preprint (arXiv: 2004.06724)
Vacca W. D., Garmany C. D., Shull J. M., 1996, ApJ, 460, 914
Veilleux S., Cecil G., Bland-Hawthorn J., 2005, ARA&A, 43, 769
Veilleux S., Maiolino R., Bolatto A. D., Aalto S., 2020, A&AR, 28, 2
Walker D. L. et al., 2018, MNRAS, 474, 2373
Walker D. L., Longmore S. N., Bastian N., Kruijssen J. M. D., Rathborne J. M., Jackson J. M., Foster J. B., Contreras Y., 2015, MNRAS, 449, 715
Walker D. L., Longmore S. N., Bastian N., Kruijssen J. M. D., Rathborne J. M., Galván-Madrid R., Liu H. B., 2016, MNRAS, 457, 4536
Walsh A. J. et al., 2011, MNRAS, 416, 1764
Walsh A. J., Lo N., Burton M. G., White G. L., Purcell C. R., Longmore S. N., Phillips C. J., Brooks K. J., 2008, Publ. Astron. Soc. Aust., 25, 105
Weaver R., McCray R., Castor J., Shapiro P., Moore R., 1977, ApJ, 218, 377
Williams R. J. R., Bisbas T. G., Haworth T. J., Mackey J., 2018, MNRAS, 479, 2016
Wink J. E., Wilson T. L., Bieging J. H., 1983, A&A, 127, 211
Yusef-Zadeh F., Muno M., Wardle M., Lis D. C., 2007, ApJ, 656, 847
Zhang S. et al., 2015, ApJ, 815, 132

SUPPORTING INFORMATION

Supplementary data are available at *MNRAS* online.

final.cds
final.csv
final.fits
final.tex

Please note: Oxford University Press is not responsible for the content or functionality of any supporting materials supplied by the authors. Any queries (other than missing material) should be directed to the corresponding author for the article.

APPENDIX: PRESSURE COMPONENTS

In this section, we provide the values of the $P_{\rm H\,II}$, $P_{\rm dir}$, and $P_{\rm IR}$ pressure components determined within the four Galactic Centre H II regions; Sgr B2, G0.6, Sgr B1, and G0.3. These values form the basis of much of the analysis presented within this work, and are plotted as points in Figs 3, 4, 6, and 8. Table A1 gives each of the pressure components and the effective radius over which they have been measured either by the literature works (see Table 2), or from the source identification routine presented in this work (see Sections 2.1.2 and 2.1.3). Missing values within the table represent where the measurement set is not available to determine the pressure component; e.g. in the case of sources only identified in the high-resolution radio observations taken from the literature. In this table, we provide the dust reprocessed emission pressure using the extinction determined along each line of sight ($P_{\rm IR}$), and using a constant visual extinction of $A_{\rm V} = 20$ mag ($P_{\rm IR}(20\,{\rm mag})$; see Section 2.1.3). Missing values within these columns can indicate where the extinction is too high to accurately correct within the dust-modelling routine (see Section 2.1.3). The full, machine-readable version of Table A1 can be obtained from the supplementary online material of this work.

Table A1. The discrete measurements of the pressure calculated from sources identified from various resolution radio data sets that have been taken from the literature (see Table 2), or from the sources identified within the available infrared observations (see Sections 2.1.2 and 2.1.3). Given in columns is the source, the source id, the direct radiation pressure ($P_{\rm dir}$; Section 2.1.2), the warm ionized gas pressure ($P_{\rm H\,II}$; Section 2.1.1), the dust reprocessed emission pressure ($P_{\rm IR}$; Section 2.1.3), and literature reference. Missing values within the table represent where the measurement set is not available to determine the pressure component; e.g. in the case of $P_{\rm IR}$ for sources only identified in the high-resolution radio observations taken from the literature. In this table, we quote the dust reprocessed emission pressure using the extinction determined along each line of sight ($P_{\rm IR}$), and using a constant visual extinction of $A_{\rm V} = 20$ mag ($P_{\rm IR}(20\,{\rm mag})$; see Section 2.1.3). Missing values within these columns can indicate where the extinction is too high to accurately correct within the dust-modelling routine (see Section 2.1.3). The full, machine-readable version of this table can be obtained from the supplementary online material.

Source	id	$R_{\rm eff}$ pc	$\log(P_{\rm dir}/k_{\rm B})$ K cm^{-3}	$\log(P_{\rm HII}/k_{\rm B})$ K cm^{-3}	$\log(P_{\rm IR}/k_{\rm B})$ K erg^{-1}	$\log(P_{\rm IR}(20\,{\rm mag})/k_{\rm B})$ K erg^{-1}	reference
SgrB2	1	1.447	6.367	...	...	...	This work
SgrB2	2	3.235	6.210	...	...	5.126	This work
SgrB2	3	1.402	6.508	...	...	5.984	This work
SgrB2	4	2.322	6.573	...	...	5.917	This work
SgrB2	5	1.652	6.530	...	...	5.376	This work
SgrB2	6	1.447	6.610	...	...	5.396	This work
SgrB2	2	0.038	9.054	8.158	...	...	Schmiedeke et al. (2016)
SgrB2	3	0.025	9.559	8.609	...	...	Schmiedeke et al. (2016)
SgrB2	4	0.007	10.067	8.582	...	...	Schmiedeke et al. (2016)
SgrB2	5	0.010	9.877	8.533	...	...	Schmiedeke et al. (2016)
SgrB2	6	0.010	9.856	8.501	...	...	Schmiedeke et al. (2016)
SgrB2	7	0.017	9.583	8.439	...	...	Schmiedeke et al. (2016)
SgrB2	8	0.009	9.958	8.615	...	...	Schmiedeke et al. (2016)
SgrB2	9	0.007	10.105	8.667	...	...	Schmiedeke et al. (2016)
SgrB2	10	0.029	9.267	8.305	...	...	Schmiedeke et al. (2016)
SgrB2	11	0.021	9.530	8.493	...	...	Schmiedeke et al. (2016)
SgrB2	12	0.038	9.226	8.362	...	...	Schmiedeke et al. (2016)
SgrB2	13	0.004	11.226	9.822	...	...	Schmiedeke et al. (2016)
SgrB2	14	0.002	12.004	10.260	...	...	Schmiedeke et al. (2016)
SgrB2	15	0.003	11.418	9.920	...	...	Schmiedeke et al. (2016)
SgrB2	16	0.001	12.277	10.350	...	...	Schmiedeke et al. (2016)
SgrB2	17	0.004	11.140	9.736	...	...	Schmiedeke et al. (2016)
SgrB2	18	0.004	11.141	9.920	...	...	Schmiedeke et al. (2016)
SgrB2	19	0.002	11.609	10.248	...	...	Schmiedeke et al. (2016)
SgrB2	20	0.002	11.705	9.963	...	...	Schmiedeke et al. (2016)
SgrB2	21	0.002	11.472	9.884	...	...	Schmiedeke et al. (2016)
SgrB2	22	0.002	11.329	9.910	...	...	Schmiedeke et al. (2016)
G0.6	1	1.708	6.266	...	...	4.686	This work
G0.6	2	1.098	6.517	...	...	5.997	This work
G0.6	3	1.402	6.566	...	...	5.901	This work
G0.6	4	0.666	6.504	...	5.901	5.437	This work
G0.6	5	2.959	6.683	...	...	5.829	This work
G0.6	6	1.380	6.596	...	...	5.460	This work
G0.6	1	0.058	8.626	8.065	...	...	Mehringer et al. (1992)
G0.6	2	0.058	8.707	8.176	...	...	Mehringer et al. (1992)
G0.6	3	0.062	8.891	8.384	...	...	Mehringer et al. (1992)
G0.6	4	0.062	8.510	7.935	...	...	Mehringer et al. (1992)
SgrB1	1	1.181	6.379	...	...	...	This work
SgrB1	2	1.690	6.913	...	6.732	6.559	This work
SgrB1	3	0.942	6.957	...	6.695	6.404	This work
SgrB1	4	1.652	6.588	...	6.696	5.845	This work
SgrB1	5	1.039	6.931	...	6.798	6.464	This work
SgrB1	6	0.504	6.828	...	6.334	6.051	This work
SgrB1	7	1.425	6.932	...	6.789	6.531	This work
SgrB1	1	0.058	8.311	7.618	...	...	Mehringer et al. (1992)
SgrB1	2	0.388	7.112	7.007	...	...	Mehringer et al. (1992)
SgrB1	3	0.039	8.688	7.917	...	...	Mehringer et al. (1992)
SgrB1	4	0.078	8.348	7.838	...	...	Mehringer et al. (1992)
SgrB1	5	0.271	7.369	7.172	...	...	Mehringer et al. (1992)
SgrB1	6	0.062	8.054	7.284	...	...	Mehringer et al. (1992)
G0.3	1	1.181	6.749		6.299	6.029	This work
G0.3	2	0.756	6.734		6.648	5.978	This work
G0.3	3	2.336	6.727		6.299	6.009	This work
...	...	...	...	...	...	...	...

This paper has been typeset from a TEX/LATEX file prepared by the author.